HERMES-Internal 03-0xx

Target Calibrations in HERMES 2002 Running and Study of the Influence of the New Correction Coil to the HERMES Acceptance

Zhenyu Ye[1]
University of Science & Technology of China
Hefei, P.R.China

[1]yezhenyu@mail.desy.de

Abstract

An internal polarized gaseous hydrogen/deuteron target is used in the HERMES experiment to study the spin structure of the nucleus. In this document, fundamental knowledge of the high frequency transition units and sextupole magnets is introduced first, which forms the basis of the polarized gaseous hydrogen/deuteron targets. Then the experimental setup of the HERMES hydrogen target is described. After that the thesis presents most of the author's work on the HERMES hydrogen target.

The calibration procedures of the HERMES target gas analyzer (TGA) are introduced, including the TGA emission current scan, background pressure calibration, rest gas calibration, ballistic flux calibration and temperature scan. The results from the HERMES 2002 running are summarized which are are used in the HERMES data production.

During the HERMES 2002 running, a 1% beam-induced target depolarization was observed. To compensate this effect, a correction coil which surrounds the target cell was designed by the Ferrara group. To study the influence of the correction coil to the acceptance of the HERMES spectrometer, two sets of 1000,000 inclusive DIS (deep inelastic scattering) Monte Carlo events are produced, one with coil and the other without coil, to make sure there is not a bad surprise by adding a scattering center in the HERMES experiment. By comparing the respective distributions of the reconstructed kinematics, it is found that the correction coil has only little influence to the HERMES acceptance of the scattered positrons, namely around 0.1% events are lost and the bias to the reconstructed kinematic distributions is less than 0.3%. Consequently the HERMES council decided to install the correction coil in the 2003 HERA shutdown.

Contents

Chapter 1

Introduction

The HERMES experiment[1, 2, 3] is running at the HERA storage ring at DESY since 1995. It was designed to mainly study the spin structure of the nucleons by positron-nucleon *Deep Inclusive Scattering* using the longitudinally polarized positron[1] beam in the HERA storage ring and internal gaseous targets at the HERMES experiment. The schematic view of the HERMES experiment at the HERA storage ring is shown in Fig. 1.1.

The first phase[3] of the HERMES data taking covered the years 1995 to 2000. Data was taken with longitudinally polarized targets of ^3He (1995), hydrogen (1996-1997) and deuterium (1998-2000), and with unpolarized gaseous targets(H_2, D_2, ^3He, ^4He, N_2, Ne and Kr). The setup of the HERMES spectrometer[4] is shown in Fig. 1.2. After upgrade of the HERA storage ring and the HERMES spectrometer in 2000/2001, the second phase of HERMES data taking has begun and will cover the years 2002 to 2006. It will concentrate first on measurements with a transversely polarized hydrogen target for a first determination of the transversity distribution and secondly on measurements with high density unpolarized hydrogen targets to

[1]It is also possible to store electron beams in the HERA ring, but because most of the HERMES data have been taken with positron beams, for simplicity the term positron is used for both electron and positron throughout the whole thesis.

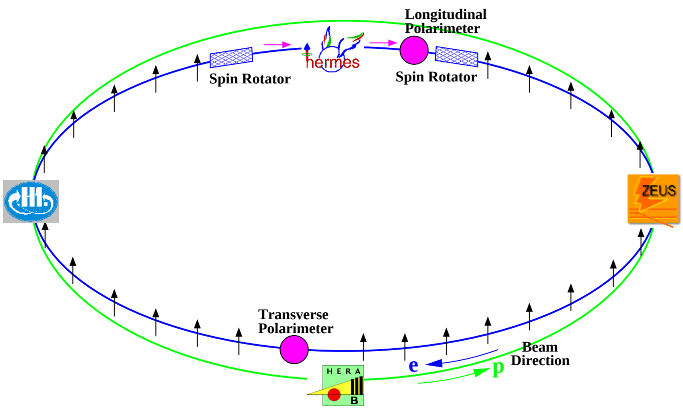

Figure 1.1: HERMES experiment and the other 3 experiments at the HERA ring.

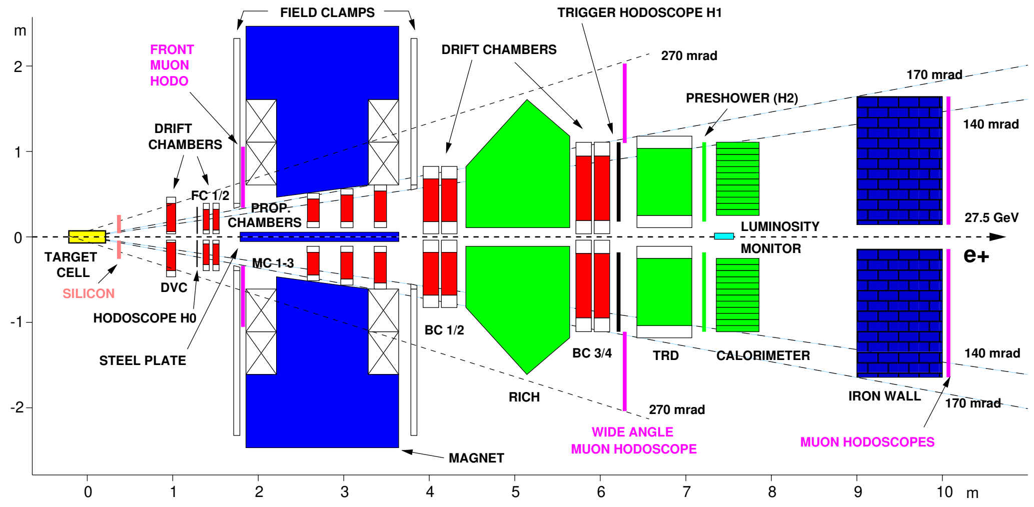

Figure 1.2: Sideview of the HERMES spectrometer.

study exclusive processes by the help of the new installed Lambda Wheel detector[5] and the Recoil detector[6] which is planned to be installed in 2004.

There are two novel features in the HERMES experiment:

- Longitudinally highly polarized positron beam
  Because of the Sokolov-Ternov[7] mechanism, the charged particle beams in the storage rings are transversely polarized. To achieve longitudinally polarized positron beam, two spin rotators[8] up- and downstream the HERMES experiment are used to rotate the polarization direction of the positron beam. A longitudinal polarimeter[9] near the HERMES experiment measures the beam polarization continuously. The average beam polarization is measured to be around 0.55.

- Polarized gaseous target internal to the storage ring
  From the experience of the EMC experiment[10] it was found that major limitations came from the high dilution factor and 8 hours polarization reversal time of the EMC solid targets. Thus gaseous targets are decided to used in the HERMES experiment with the features of no dilution ($f = 1$) for H/D atoms, high polarization ($P > 0.7$) and rapid polarization reversal in milliseconds. With the *storage cell* technology, the magnitude of the target thickness is increased by two orders compared with a free jet target. Internal polarized gaseous targets in storage rings have also been used by other recent experiments at IUCF[11] and at COSY[12].

The HERMES polarized gaseous target consists of: *Atomic Beam Source* (ABS) to provide polarized H/D atomic beams; *Storage Cell* to increase the target density; *Breit-Rabi Polarimeter* (BRP) to measure the target polarization continuously; *Target Gas Analyzer* (TGA) to measure the atomic and molecular relative contents of the target.

This thesis is structured in the following way:

- In the rest of this chapter fundamental knowledge of the high frequency transitions[2] and sextupole magnets is introduced, which form the basis of the polarized gaseous hydrogen/deuteron targets;
- The 2nd chapter describes the HERMES target experimental setup;
- In chapter 3 calibrations for the TGA of the HERMES hydrogen target in the HERMES 2002 running are summarized;
- In chapter 4 the study on the influence of the new correction coil to the HERMES acceptance are presented as a part of author's work for the HERMES target group.
- In the last chapter the conclusions are presented.

[2]As the knowledge has been studied for a long time and is well understood in some literatures, some parts are taken from the reference papers.

1.1 Hyperfine Structure of Hydrogen/Deuterium

The hyperfine structure of hydrogen/deuterium atoms can be derived from Hamilton operators, which describe the coupling of the electron spin $\vec{S}$ with the nucleus spin $\vec{I}$ and the interaction of their magnetic moments with the external magnetic field $\vec{B}$:

$$\mathcal{H} = \mathcal{A}_{H,D}\vec{S}\cdot\vec{I} + \frac{g_S\mu_B}{\hbar}\vec{S}\cdot\vec{B} - \frac{g_I\mu_N}{\hbar}\vec{I}\cdot\vec{B} \tag{1.1}$$

The first term $\mathcal{A}_H$ ($\mathcal{A}_D$)[14] is a measure of the coupling strength between $\vec{S}$ and $\vec{I}$ for hydrogen (deuterium), g_S (g_I) is the gyromagnetic factor of electron (nucleus). $\mathcal{A}_{H,D}$ can be calculated using the following approximate formula:

$$\mathcal{A}_{H,D} = \frac{2}{3}g_s g_{p,d}\frac{m_e}{m_p}m_e c^2\alpha^4\left(1+\frac{m_e}{m_p}^{-3}\right)\frac{1}{\hbar^2} \tag{1.2}$$

in which α is the fine structure constant, m_e is the mass of electron, m_p is the mass of proton, g_p and g_d are the gyromagnetic factors of the proton and deuteron respectively and c is the speed of light. In case of hydrogen where $S = I = \frac{1}{2}$ the coupling $\vec{S}\cdot\vec{I}$ originates a singlet state with $F = 0$ and a triplet with $F = 1\,(m_F = \pm 1)$. In case of deuterium $S = \frac{1}{2}$ and $I = 1$, so that a doublet $F = \frac{1}{2}\left(m_F = \pm\frac{1}{2}\right)$ and a quadruplet $F = \frac{3}{2}\left(m_F = \pm\frac{3}{2}, \pm\frac{1}{2}\right)$ are produced from the spin-spin coupling.

A basis for the Hamilton operator is given by the product wave functions[3] $|\uparrow +\rangle$, $|\uparrow -\rangle$, $|\downarrow +\rangle$ and $|\downarrow -\rangle$ for hydrogen ($|\uparrow 1\rangle$, $|\uparrow 0\rangle$, $|\uparrow -1\rangle$, $|\downarrow 1\rangle$, $|\downarrow 0\rangle$ and $|\downarrow -1\rangle$ for deuterium). From the basis one can find the eigenvectors and eigenenergies of $\mathcal{H}$ by an orthogonal transformation. Fig. 1.3 shows the energy levels of hydrogen and deuterium as a function of the magnetic holding field. The energy and field values are scaled with the corresponding values of E_{HFS} and B_C respectively which are defined by:

[3] the arrow refers to the electron spin

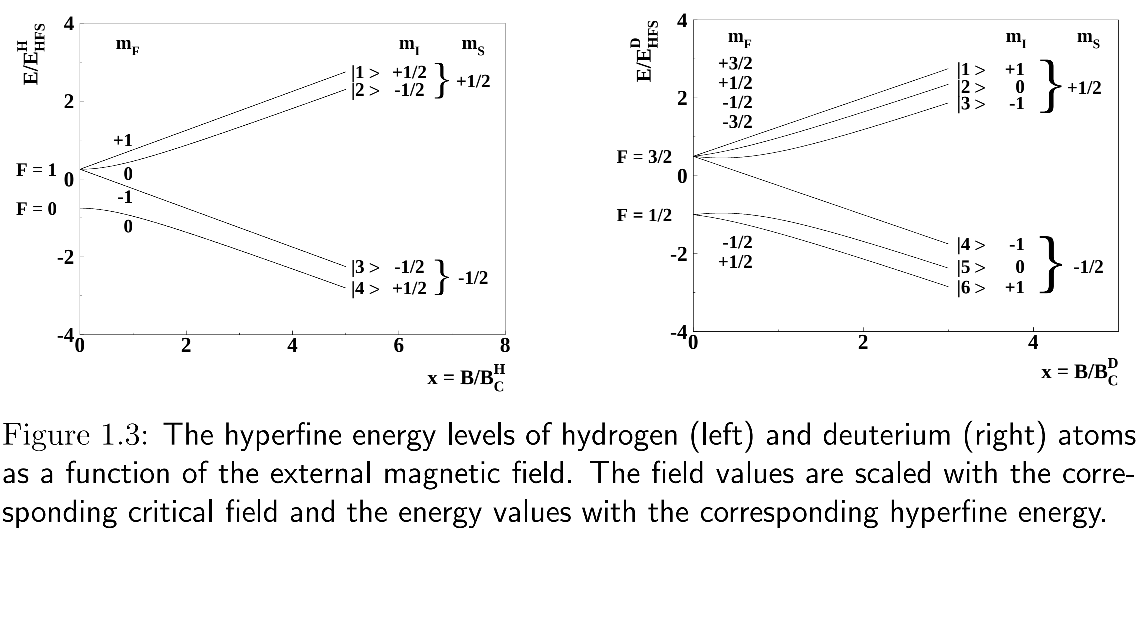

Figure 1.3: The hyperfine energy levels of hydrogen (left) and deuterium (right) atoms as a function of the external magnetic field. The field values are scaled with the corresponding critical field and the energy values with the corresponding hyperfine energy.

$$
\begin{aligned}
E^H_{HFS} &= \mathcal{A}_H \hbar^2 \simeq 2\pi\hbar\, 1.42GHz & E^D_{HFS} &= \mathcal{A}_H \hbar^2 \simeq 2\pi\hbar\, 0.327GHz \\
B^H_C &= E_H F S^H / g_S \mu_B \simeq 50.7mT & B^D_C &= E^H_{HFS} / g_S \mu_B \simeq 11.7mT
\end{aligned}
$$

The Breit-Rabi basis consists of eigenvectors of $\mathcal{H}$, which is denoted as $|\,1\,\rangle \ldots |\,4\,\rangle$ (resp. $|\,1\,\rangle \ldots |\,6\,\rangle$ for deuterium). They are given by:

Hydrogen

$$
\begin{aligned}
|\,1\,\rangle &= |\uparrow +\rangle \\
|\,2\,\rangle &= \cos\theta\,|\uparrow -\rangle + \sin\theta\,|\downarrow +\rangle \\
|\,3\,\rangle &= |\downarrow -\rangle \\
|\,4\,\rangle &= -\sin\theta\,|\uparrow -\rangle + \cos\theta\,|\downarrow +\rangle
\end{aligned}
$$

Deuterium

$$
\begin{aligned}
|\,1\,\rangle &= |\uparrow +1\,\rangle \\
|\,2\,\rangle &= \cos\theta_+\,|\uparrow 0\,\rangle + \sin\theta_+\,|\downarrow +1\,\rangle \\
|\,3\,\rangle &= \cos\theta_-\,|\uparrow -1\,\rangle + \sin\theta_-\,|\downarrow 0\,\rangle \\
|\,4\,\rangle &= |\downarrow -1\,\rangle \\
|\,5\,\rangle &= -\sin\theta_-\,|\uparrow -1\,\rangle + \cos\theta_-\,|\downarrow 0\,\rangle \\
|\,6\,\rangle &= -\sin\theta_+\,|\uparrow 0\,\rangle + \cos\theta_+\,|\downarrow +1\,\rangle
\end{aligned}
$$

The mixing angles θ, θ_+ and θ_- are functions of the magnetic holding field $B = B_z$, as listed in Tab. 1.1. The holding field can be expressed by the dimensionless Breit-Rabi variable $x = \frac{B_z}{B_C}$.

Using the hyperfine population numbers N_a, which represent the occupation of atoms in each state $|\,a\,\rangle$, the electron and nuclear polarizations (P_e and P_z) are given by the expectation values of the operators S_z and I_z respectively, which are,
for hydrogen:

$$
\begin{aligned}
P_e &= N_1 - N_3 + (N_2 - N_4)\cos 2\theta \\
P_z &= N_1 - N_3 - (N_2 - N_4)\cos 2\theta
\end{aligned}
\tag{1.3}
$$

and for deuterium [4]:

[4] As the deuteron has 3 states $m_I = 1, 0, -1$, its spin state is not completely characterized by the value of the vector polarization P_z. In addition to P_z one often uses the tensor polarization P_{zz}, which is defined ad the $z - z$ component of the tensor operator $I_{ij} = \frac{3}{2}(I_i I_j + I_j I_i) - 2\delta_i j$. The tensor polarization of the deuteron is given by:

$$
\begin{aligned}
P_{zz} &= \langle I_{zz} \rangle = \left\langle 3I_z^2 - 2 \right\rangle \\
&= N_1 + N_4 - \frac{1}{2}N_2\left(3\cos 2\theta_+ + 1\right) + \frac{1}{2}N_3\left(3\cos 2\theta_- - 1\right) \\
&\quad -\frac{1}{2}N_5\left(3\cos 2\theta_- + 1\right) + \frac{1}{2}N_6\left(3\cos 2\theta_+ - 1\right)
\end{aligned}
$$

Hydrogen	Deuterium
$\cos\theta = \sqrt{\frac{1}{2}\left(1+\cos 2\theta\right)}$ $\sin\theta = \sqrt{\frac{1}{2}\left(1-\cos 2\theta\right)}$ $\cos 2\theta = \frac{x(1+\epsilon)}{\sqrt{x^2(1+\epsilon)^2+1}}$ $\sin 2\theta = \frac{1}{\sqrt{x^2(1+\epsilon)^2+1}}$	$\cos\theta_\pm = \sqrt{\frac{1}{2}\left(1+\cos 2\theta_\pm\right)}$ $\sin\theta_\pm = \sqrt{\frac{1}{2}\left(1-\cos 2\theta_\pm\right)}$ $\cos 2\theta_\pm = \frac{3x(1+2\epsilon)\pm1}{\sqrt{(3x(1+2\epsilon)\pm1)^2+8}}$ $\sin 2\theta_\pm = \frac{\sqrt{8}}{\sqrt{(3x(1+2\epsilon)\pm1)^2+8}}$
$E_1 = \frac{E^H_{HFS}}{4}\left(1+2x\left(1-\epsilon\right)\right)$ $E_2 = \frac{E^H_{HFS}}{4}\left(-1+2\sqrt{x^2\left(1+\epsilon\right)^2+1}\right)$ $E_3 = \frac{E^H_{HFS}}{4}\left(1-2x\left(1-\epsilon\right)\right)$ $E_4 = \frac{E^H_{HFS}}{4}\left(-1-2\sqrt{x^2\left(1+\epsilon\right)^2+1}\right)$	$E_1 = \frac{E^D_{HFS}}{3}\left(1+\frac{3}{2}x\left(1-2\epsilon\right)\right)$ $E_2 = \frac{E^D_{HFS}}{6}\left(-1+\sqrt{9x^2\left(1+2\epsilon\right)^2+6x\left(1+2\epsilon\right)+9}\right)$ $E_3 = \frac{E^D_{HFS}}{6}\left(-1+\sqrt{9x^2\left(1+2\epsilon\right)^2-6x\left(1+2\epsilon\right)+9}\right)$ $E_4 = \frac{E^D_{HFS}}{3}\left(1-\frac{3}{2}x\left(1-2\epsilon\right)\right)$ $E_5 = \frac{E^D_{HFS}}{6}\left(-1-\sqrt{9x^2\left(1+2\epsilon\right)^2-6x\left(1+2\epsilon\right)+9}\right)$ $E_6 = \frac{E^D_{HFS}}{6}\left(-1-\sqrt{9x^2\left(1+2\epsilon\right)^2+6x\left(1+2\epsilon\right)+9}\right)$
$E^H_{HFS} = \mathcal{A}_H\hbar^2$	$E^D_{HFS} = \frac{3}{2}\mathcal{A}_D\hbar^2$

Table 1.1: Mixing angles and eigen-energies of the hyperfine states of hydrogen/deuterium

$$
\begin{aligned}
P_e &= N_1 - N_4 + (N_2 - N_6)\cos 2\theta_+ + (N_3 - N_5)\cos 2\theta_- \\
P_z &= N_1 + N_6 - N_3 - N_4 + (N_2 - N_6)\sin^2 2\theta_+ + (N_3 - N_5)\sin^2\theta_-
\end{aligned}
\tag{1.4}
$$

1.2 Hyperfine Transitions[5]

High Frequency Transition (HFT) units are used to exchange the hyperfine states of atoms in one or several steps. This exchange is required to transfer the polarization of the electrons to the nucleons. Additionally hyperfine transitions cause depolarization during wall collisions and by resonant depolarization induced by the bunch field of the HERA positron beam. Let us consider an external magnetic field having the following form:

$$\vec{B} = \left(0, 0, B^{st} + b(t)\right) \tag{1.5}$$

Each hyperfine transition has a correspondent frequency μ_{ab}, related to the energy difference $E_a - E_b$ of the transition $a \leftrightarrow b$:

$$\mu_{ab} = \frac{|E_a - E_b|}{2\pi\hbar} \tag{1.6}$$

[5]Most of this section coming from [13]

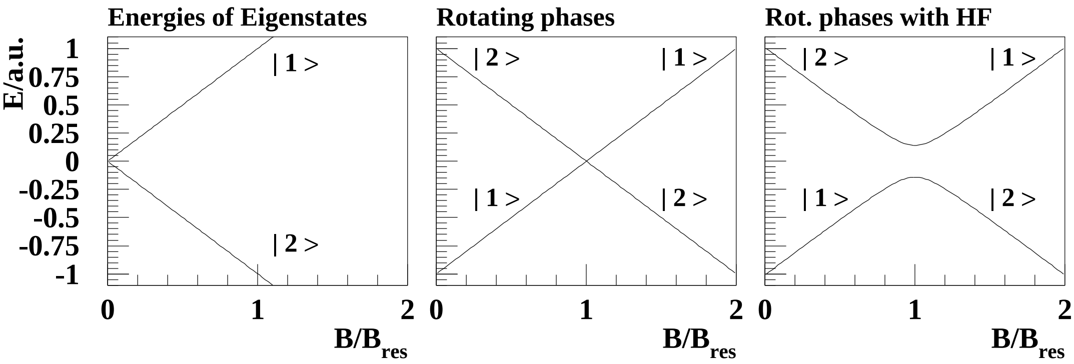

Figure 1.4: schematic diagram of the adiabatic passsage through a resonance.Left: Eigenergies of two hyperfine states in linear approximation versus the holding field (relative to the field value of the resonance B_{res}).

The frequencies of the hyperfine transitions depend on the magnetic holding field. Therefor the operation of a HFT requires a careful tuning of either the frequency and/or of the magnetic field, in order to obtain an optimal transition efficiency. Usually one distinguishes hyperfine transitions with $\Delta m_F = 0$ from those with $\Delta m_F = 1$ and those with $\Delta F = 1$ from those with $\Delta F = 0$. Tab. 1.2 summarizes the different transition types. *Strong Field Transition* (SFT) are characterized by $\Delta m_F = 1$, *Weak and Medium field Transitions* (WFT/MFT)[15][6] by $\Delta m_F = 0$. SFTs usually run with a frequency higher than $\mu_{HFS} = E_{HFS}/h$, while the transition frequency of a WFT/MFT is – in the limiting case of $B_z \rightarrow 0$ – proportional to the field. SFTs are realized by resonator cavities and WFTs/MFTs by high frequency coils. The cavities have to be replaced for a change of the target gas from hydrogen to deuterium because the cavities are tuned to a fixed frequency. A high frequency field parallel to the static field can be used to introduce transitions with $\Delta m_F = 0$ between the mixed states, a high frequency field perpendicular to the static field can induce transitions with $\Delta m_F = 1$. If an atom stays in resonance with a magnetic high frequency field, the spin starts to oscillate between the two eigen-states $|\, a\, \rangle$ and $|\, b\, \rangle$. An efficient exchange of two hyperfine states can be realized with a so-called *adiabatic transition.* A field gradient along the axis of the atomic beam guarantees, that the atoms passes the resonance conditions exactly once. If an atom that moving along the gradient field from either low to high field values, stays in its adiabatic eigen-states, the transition efficiency is ideally 100% as showed in Fig. 1.4. Practical efficiencies of more than 98% can be reached with resonant regions of a few *cm* length for atoms of thermal velocity.

[6]Some authors have chosen a different notation for the transition types. For example, Philpott named transitions with $\Delta F = 1$ MFT and those with $\Delta F = 0$ WFT. In this thesis, the meaning of MFT is a transition with $\Delta m_F = 0$ in the physical context, in a technical context, it is a combination of one or several subsequent physical MFTs, operated as single-photon transitions. A WFT is a special way to run a cascade of MFTs in a multi-photon mode. In case of hydrogen, it was found that the effect of the WFT can be described reasonably well by a direct exchange between state $|\, 1\, \rangle$ and $|\, 3\, \rangle$ with one efficiecy only[13]

Orientation	σ/π	Type	Δm_F	ΔF	Δm_I	Δm_S	Hydrogen	Deuterium
$B(t)\|\|B^{st}$	σ	SFT	0	±1	±1	±1	2$\leftrightarrow$4	2$\leftrightarrow$6
$B(t)\|\|B^{st}$	σ	SFT	0	±1	±1	±1		2$\leftrightarrow$6
$B(t)\|\|B^{st}$	σ	SFT	0	±1	±1	±1		2$\leftrightarrow$6
$B(t)\perp B^{st}$	π	SFT	±1	±1	0	±1	1$\leftrightarrow$4	1$\leftrightarrow$6
$B(t)\perp B^{st}$	π	SFT	±1	±1	0	±1		2$\leftrightarrow$5
$B(t)\perp B^{st}$	π	SFT	±1	±1	±2	±1		3$\leftrightarrow$6
$B(t)\perp B^{st}$	π	SFT	±1	±1	±1	0	3$\leftrightarrow$4	4$\leftrightarrow$5
$B(t)\perp B^{st}$	π	MFT	±1	0	±1	0	1$\leftrightarrow$2	1$\leftrightarrow$2
$B(t)\perp B^{st}$	π	MFT	±1	0	±1	0		2$\leftrightarrow$3
$B(t)\perp B^{st}$	π	MFT	±1	0	±1	0		5$\leftrightarrow$6
$B(t)\perp B^{st}$	π	MFT	±1	0	0	±1	2$\leftrightarrow$3	
$B(t)\perp B^{st}$	π	MFT	±1	0	0	±1		3$\leftrightarrow$4

Table 1.2: Hyperfine transitions of hydrogen and deuterium and their features. Transitions with $\Delta F = 1$ are called Strong Field Transitions, transitions with $\Delta F = 0$ are called medium field transitions. Transitions with $\Delta m_F = 0$ are called σ–transitions, those with $\Delta m_F = 1$ are called π–transitions.

If one uses the vector of hyperfine population numbers $N_a = (N_1, N_2, \cdots)^T$ for the description of an atomic sample, the effect of a HFT on the hyperfine population can be described by a Matrix T_{ab}:

$$N_a \rightarrow \sum_b T_{ab} N_b \tag{1.7}$$

This matrix can be written as – in case of a SFT $2 \leftrightarrow 4$ transition of hydrogen:

$$T_{24} = \begin{pmatrix} 1 & 0 & 0 & 0 \\ 0 & 1-\epsilon_{42} & 0 & \epsilon_{42} \\ 0 & 0 & 1 & 0 \\ 0 & \epsilon_{24} & 0 & 1-\epsilon_{24} \end{pmatrix} \tag{1.8}$$

where $\epsilon_{24} = \epsilon_{42}$ is the efficiency of the transition. Medium and weak field transitions have to be modelled by subsequent separate transitions, each with an individual transition efficiency. The order of the matrix multiplications depends on the sign of the gradient field. For example, a hydrogen weak field $1 \leftrightarrow 4$ transition with positive gradient can be described by:

$$T^{WFT} = T_{12} \cdot T_{13} \cdot T_{23} \tag{1.9}$$

1.2.1 Strong Field Transitions

In a SFT unit, which is designed for σ transitions only[7], the hydrogen hamiltonian for the adiabatic passage has the following form:

$$\mathcal{H}_2^{SFT} = \begin{pmatrix} E_1 - \frac{1}{4}\hbar\omega & 0 & 0 & 0 \\ 0 & E_2 - \frac{1}{4}\hbar\omega & 0 & \hbar A \\ 0 & 0 & E_3 - \frac{1}{4}\hbar\omega & 0 \\ 0 & \hbar A & 0 & E_4 + \frac{3}{4}\hbar\omega \end{pmatrix} \tag{1.10}$$

with $A = y_\sigma \frac{\omega_{HFS}}{2} \sin 2\theta$. As expected, only the states $|\,2\,\rangle$ and $|\,4\,\rangle$ are involved in the transition and have to diagonalized by a new orthogonal transformation U_2. Ignoring the unaffected states, the Schrödinger equation can be written as:

$$i \begin{pmatrix} \dot{\phi}_2 \\ \dot{\phi}_4 \end{pmatrix} = \begin{pmatrix} \omega_2 - \frac{1}{4}\omega & A \\ A & \omega_4 + \frac{3}{4}\omega \end{pmatrix} \cdot \begin{pmatrix} \phi_2 \\ \phi_4 \end{pmatrix} \tag{1.11}$$

The orthogonal transformation U_2 is given by

$$\begin{array}{cc} U_2 = \begin{pmatrix} c & s \\ -s & c \end{pmatrix}, & c = \sqrt{\frac{1}{2}(1+\delta)} \\ s = \sqrt{\frac{1}{2}(1-\delta)} \quad , & \delta = \frac{\omega - \omega_{24}}{\sqrt{(\omega-\omega_{24})^2 + 4A^2}} \end{array} \tag{1.12}$$

As shown in Fig. 1.3, the transitions frequency $\omega_{24} = \omega_2 - \omega_4$ increases monotonically with the static field. If the atom passes the resonance $\omega = \omega_{24}$ within the high frequency resonator by means of travelling along an increasing static field, the values of δ, c and s change with time as shown in the left graph of Fig. 1.5. The right graph shows the eigen-energies without high frequency field (thin lines) and with the high frequency field switched on (thick lines). If the passage through the resonance is slow enough[8], the atoms stay on the thick lines and the population of the hyperfine states is exchanged. As the other hyperfine states $|\,1\,\rangle$ and $|\,3\,\rangle$ are not involved, the effect can be described by one parameter - the exchange efficiency ϵ_{24}[9]. The

[7] This is the case for the SFT units of the HERMES ABS, while the SFT unit of the BRP has tilted resonators, that allow to run both σ transition and π transition simultaneously.

[8] The condition is given by the requirement, that the distortion term $\hbar \dot{U}_2^T U_2$ is small compared to the adiabatic eigen-energies.

[9] Due to the symmetry of the eigen-energies as a function of time/field as shown in Fig. 1.5, the efficiency should be symmetric: $\epsilon_{24} = \epsilon_{2\to4} = \epsilon_{4\to2}$

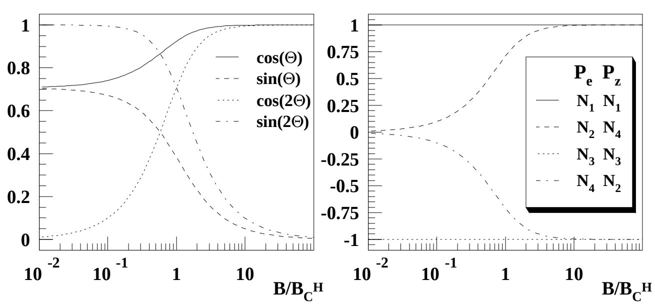

Figure 1.5: The dependence of mixing angle (left) and polarization (right) for hydrogen on the holding magnetic field.

efficiency of an adiabatic transition is given by $\epsilon = 1 - e^{-2\pi\kappa}$ with κ given by [16]:

$$\kappa = \left| \frac{\mu B_{HF}^2}{2\hbar \dot{B}_{stat}} \right| \tag{1.13}$$

Hence, a high efficiency requires most of all sufficient high frequency amlitude[10]:

$$\mu B_{HF}^2 \gg \left| 2\hbar \dot{B}_{stat} \right| \tag{1.14}$$

1.2.2 Weak/Medium Field Transitions

Weak and medium field transitions are in contrast to strong field transitions that WFT/MFT use not single and well separated transitions between two hyperfine states, but more complex multiple transitions. Their effect on the hyperfine population depends on the selected frequency, the amplitude of the high frequency, the strength and sign of the gradient field and is very sensitive on the selected static field. For hydrogen, the Hamilton operator $\mathcal{H}_2^{WFT}$ is given by:

$$\mathcal{H}_2^{WFT} = \begin{pmatrix} E_1 - \hbar\omega & A\sin\theta & 0 & 0 \\ A\sin\theta & E_2 & A\cos\theta & 0 \\ 0 & A\cos\theta & E_3 + \hbar\omega & 0 \\ 0 & 0 & 0 & E_4 \end{pmatrix} \tag{1.15}$$

with $A = \frac{E_{HFS}^H}{4} y$. Again the resulting operators are symmetric and real and can be diagonalized by an orthogonal transformation. Fig. 1.6 shows the resulting eigen-energies for a deuterium weak field transition at a frequency of $7MHz$ for the state $|\,1\,\rangle \ldots |\,4\,\rangle$. The resonance condition is matched for single-photon transitions at 3 points, indicated by open cycles, at two points for two-photon transitions (open squares) and at one point for a three-photon transition. One can see, that the separation of the eigen-energies and hence the efficiency depends on the multiplicity of the transition. A *medium field transition is based on the single photon transitions only, while one usually speaks only of a* weak field transition, if multiple photon transitions take place. The second graph from the left in Fig. 1.6 indicates that only the single-photon transitions $1 \leftrightarrow 2$, $2 \leftrightarrow 3$ and $3 \leftrightarrow 4$ will effectively run at this low amplitude. With a positive gradient, the transition will have the following effect on

[10]The equation could also be interpreted in the way, that $\dot{B}_{stat}$ should be as low as possible. This interpretation has to be rejected due to the following reasons: With the average velocity of the atoms (v) and the field gradient B_{grad}, one obtains: $\dot{B}_{stat} = B_{grad} \langle v \rangle$. The velocity of the atoms as well as the effective length Δl of the high frequency resonator (resp. coil) are given by the experimental circumstances. The requirement of a high efficient exchange is, that δ ranges from 1... -1 within the high frequency field, which requires, that $\Delta B = B_{grad} {\cdot} \Delta l \geq |B(\delta\ 1) - B(\delta\ -1)|$. A reduction of the gradient is possible, if the high frequency amplitude is a smooth function along the path of the atoms.

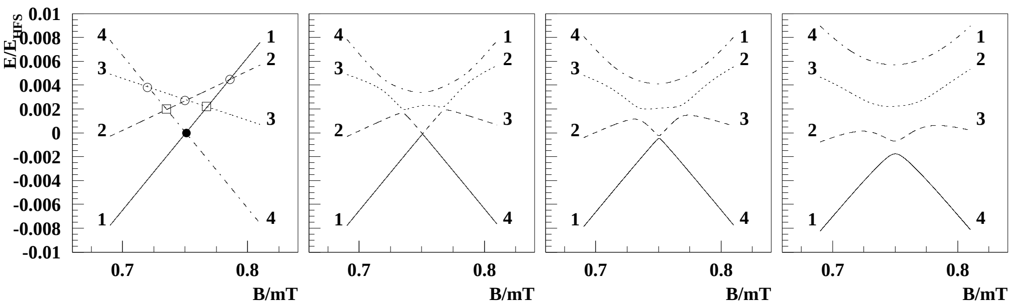

Figure 1.6: Eigen-energies of the shifted eigenstates in the adiabatic basis for a high frequency amplitude of - from left to right - 0, 0.01, 0.02 and 0.04 times the critical field and a frequency of $7MHz$. Cross points of the shifted energy levels are marked in the leftmost graph. Open circles represent single-photon, open squares double-photon and the filled circle the three-photon transition points.

the hyperfine population (state $|\,5\,\rangle$ and $|\,6\,\rangle$ can be analyzed separately):

$$\begin{pmatrix} N_1 \\ N_2 \\ N_3 \\ N_4 \end{pmatrix} \overset{1 \leftrightarrow 2}{\longrightarrow} \begin{pmatrix} N_2 \\ N_1 \\ N_3 \\ N_4 \end{pmatrix} \overset{2 \leftrightarrow 4}{\longrightarrow} \begin{pmatrix} N_2 \\ N_4 \\ N_3 \\ N_1 \end{pmatrix} \overset{2 \leftrightarrow 3}{\longrightarrow} \begin{pmatrix} N_2 \\ N_3 \\ N_4 \\ N_1 \end{pmatrix} \overset{1 \leftrightarrow 4}{\longrightarrow}$$
$$\begin{pmatrix} N_1 \\ N_3 \\ N_4 \\ N_2 \end{pmatrix} \overset{1 \leftrightarrow 3}{\longrightarrow} \begin{pmatrix} N_4 \\ N_3 \\ N_1 \\ N_2 \end{pmatrix} \overset{3 \leftrightarrow 4}{\longrightarrow} \begin{pmatrix} N_4 \\ N_3 \\ N_2 \\ N_1 \end{pmatrix}$$

In this case, one needs 3 efficiencies to describe a hydrogen weak field transition and 6 in case of deuterium. One can assume, that the single-photon transitions operate close to 100%. This reduces the required number of efficiencies to one for hydrogen and 3 for deuterium. Fig. 1.7 shows the result of a polarization measurements for different amplitudes of a deuterium WFT, that illustrates the mentioned WFT/MFT behavior. This analysis of the WFT behavior is necessary for optimization and analysis of the injected polarization.
The optimal conditions for the operation of a WFT/MFT transition therefore depend on the intended effect on the hyperfine population and the location of the transition. If, as in case of the HERMES setup for deuterium, the sextupole subsystems in combination with a SFT 3-5 prepare a hyperfine population with atoms only in state $|\,1\,\rangle$ and $|\,2\,\rangle$, and the WFT behind the sextupoles is supposed to deliver state $|\,3\,\rangle$ and $|\,4\,\rangle$ for P_{Z-} injection, then a negative gradient has to be chosen. In this case, the three photon transition is not required to run at all, as the intended population of hyperfine states $|\,3\,\rangle$ and $|\,4\,\rangle$ can also be realized with a $1 \rightarrow 3/2 \rightarrow 4$ transition instead of a $1 \rightarrow 4/2 \rightarrow 3$ transition.
In the limiting case of high rf-amplitude and low rf-frequency[11], the single photon transitions of a WFT can be assumed to run at full efficiency, so that a hydrogen WFT can be described by the efficiency ϵ_{13} and a deuterium WFT by 3 transition

[11] $14MHz$ in case of a hydrogen and $7MHz$ in case of a deuterium WFT

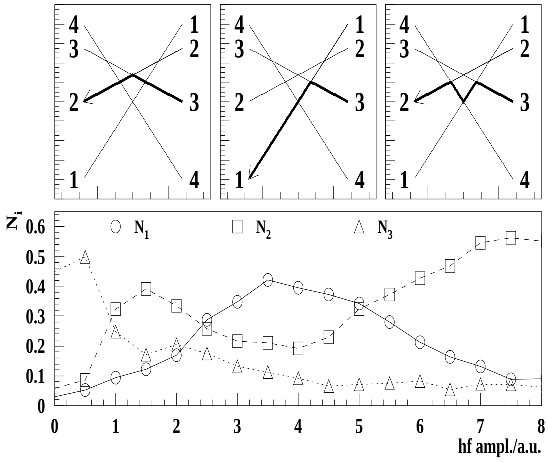

Figure 1.7: (Amplitude dependence of WFT operation with negative field gradient), measured with the deuterium WFT in the appendix of the ABS. The transitions between the sextupole were used to reject state $|\,1\,\rangle$ and $|\,2\,\rangle$. As indicated in the upper schemes, state $|\,3\,\rangle$ enters the WFT unit (from high to low field) and is transferred to state $|\,2\,\rangle$ by a single- photon transition at an amplitude of $\tilde{1}.5$, to state $|\,1\,\rangle$ with the double-photon transition at an amplitude of $\tilde{3}.5$ and again to state $|\,2\,\rangle$ at full amplitude, where the 3-photon transition runs

efficiencies (ϵ_{13}, ϵ_{14}, ϵ_{24}). In case of MFT operation, higher rf-frequencies[12] are chosen and multi-photon transitions are assumed to be negligible, so that a hydrogen MFT can be described by 2 and a deuterium MFT by 3 efficiencies.

1.3 Sextupole Magnets

The production of intense beams of polarized atoms is of great interest to the nuclear and particle community. Among the various methods employed up to the present time, Stern-Gerlach separation of atoms in inhomogeneous magnetic multipole fields, combining with high frequency transitions, is most widely used for the production of nuclear spin polarized beams of hydrogen and deuterium. In atomic beam sources systems consisting of sextupole magnets are commonly used because of their harmonic focusing properties. The magnitude of the magnetic flux density inside a sextupole of inner radius r_1 and pole-tip field B_0 at a distance r from the axis of the magnet is given by:

$$B(r) = B_0\,(r/r_1)^2 \tag{1.16}$$

The design of multipole magnets consisting of permanently magnetized segments has been described in detail in [19]. For typical geometries of the atomic beam sources the accepted beam solid angle and thus the flux of the selected particles is proportional to pole tip magnetic field. When considering the focusing properties of the magnet the one with a higher multipolarity is preferable, because it allows higher acceptance and/or flux of polarized atoms at the same value of the magnetic field. However, only quadrupole or sextupole magnets are used because of the difficulty to satisfy the above mentioned requirement for higher multipolarity - to keep the same magnetic field strength at the magnet. Also due to their harmonic focusing field sextupole magnets are preferable to focus atoms at a given position.

With the advent of a new generation of magnetic materials in 1984, developed by researchers from Sumitomo[20], energy densities $(BH)_{max} \sim 290kJ/m^3$ have been

[12] $> 50MHz$ in case of a hydrogen and $> 25MHz$ in case of a deuterium MFT

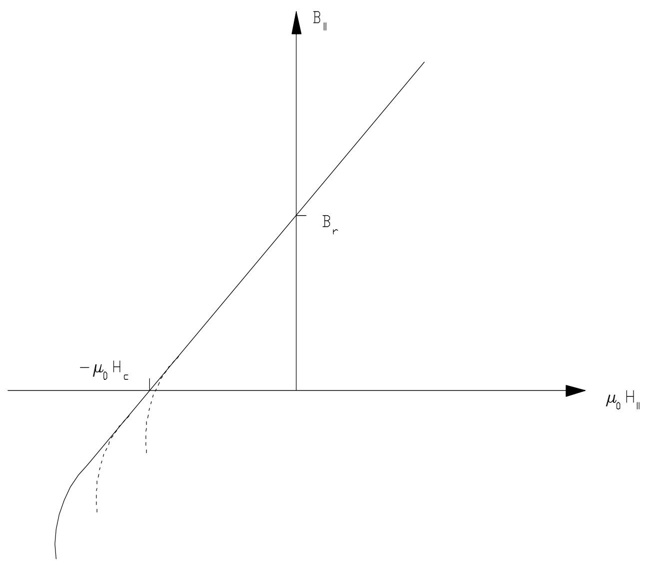

Figure 1.8: The magnetic properties of rare earth cobalt materials

achieved[21]. These new materials were subsequently used in nuclear physics to build magnet systems for ion and atomic beam sources, yielding at most pole-tip fields of $\sim 1.4T$. Modern permanent magnet materials such as VACODYM 510HR[22] reach typical energy densities of $(BH)_{max} \sim 385kJ/m^3$.

Pole-tip fields of $3.2-4.6T$ of sextupoles with inner radii of $14-44mm$ have been reported in [23] using hybrid magnets consisting of superconducting coils surrounded by an ion yoke. A superconductive sextupole system free of iron is described in [24] which generates sextupole-tip fields of $1.54T$ at an inner magnet radius of $65mm$.

In this section, the most recent yields of permanent sextupole magnets and superconducting sextupole magnets are introduced. The properties of permanent sextupole magnets at the ANKE[26] ABS and superconducting sextupole magnets at the VEPP-3[27] ABS are listed. The principle of the stern-gerlach force and the separation mechanism is described briefly.

1.3.1 Permanent Sextupole Magnet

Rare earth cobalt(REC) material, which has the advantage of strong magnetization, is used to design and produce fields that are as strong or stronger than those achievable with conventional magnets of any size. The other important advantage of REC is the simplicity of its magnetic properties, which makes REC easy to understand and to treat analytically and leads to improved designs. The relationship between $B_{||}$ and $H_{||}$ in the direction parallel to the easy axis is schematically shown in Fig. 1.8. The most important characteristics of the curve are the following:

- It is for all intents and purposes a straight line over a very wide range, with a typical slope $1.04 - 1.08$. The point where the slope becomes significantly larger depend on the manufacturing process, but lies well within the third

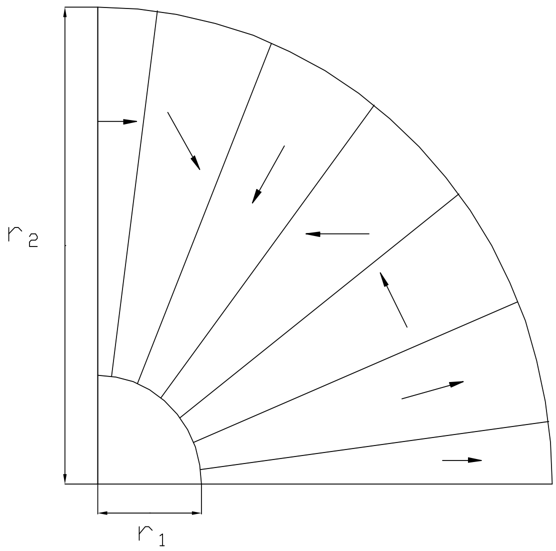

Figure 1.9: One quadrant of a cylindrically symmetric sextupole magnet consisting of 24 segment. The arrows denote the direction of magnetization.

quadrant, with $H_C \simeq 1.5 - 2$.

- The offset of the curve which is the remanent field B_t is typically $0.8 - 0.9T$ with the coercive field $\mu_0 H_C$ about $4 - 8\%$ less than it.

After a molted mixture of roughly five(atomic) parts cobalt to one(atomic) part of some rare earth metal(s) is solidified by rapid cooling, a crushing and milling process produces a powder that consists of particles with linear dimensions of the order of $5\mu m$. These grains are magnetically highly anisotropic to be polarized only along one crystalline direction. The powder is then exposed to a strong magnetic field and subjected to high pressure, causing the individual grains to physically rotate until their magnetically preferred axes are parallel to the applied field. These aligned blocks of material are then sintered and machined or ground if necessary. Finally the material is exposed to a very strong magnetic field in a direction parallel or antiparallel to the previously established preferred direction, orienting practically all alignable magnetic moments along the direction of magnetization, commonly called the easy axis.

In the range of interest here, the relationship between $B_{||}$ and $H_{||}$ can be represented by:

$$B_{||} = \mu_0 \mu_{||} H_{||} + B_r \tag{1.17}$$

In the direction perpendicular to the easy axis, the relationship between $B_\perp$ and $H_\perp$ is, to a good approximation, described by:

$$B_\perp = \mu_0 H_\perp + B_r \left(H_{\perp / H_A} = \mu_0 \mu_\perp H_{perp} \right) \tag{1.18}$$

The high degree of anisotropy of good material manifests itself in the large values of the anisotropy field $\mu_0 H_A$: typically values are $12 - 40T$, giving values of 1.02 to 1.08 for μ_{perp} and Eqn. 1.18 is usually valid up to several Tesla. A cylindrical $2N$-multipole magnet is assembled from M segments permanently magnetized such that the magnetization axis of each segment advances azimuthally by an angle $(N + 1)2\pi/M$ with respect to a fixed coordinate system, as sketched in Fig. 1.9. In

Magnet	$L(mm)$	$r_1(mm)$	$r_2(mm)$	$B_0^{HAL}(T)$	$B_0^{MAF}(T)$	$B_0^{Mea}(T)$
1	40	$5/7^a$	20	1.672	1.633	1.654(10)
2	65	$8/11^a$	32	1.680	1.641	1.684(6)
3	70	14	47	1.674	1.642	1.625(4)
4	38	15	47	1.650	1.564	1.565(2)
5	55	15	47	1.650	1.605	1.621(3)
6	55	15	47	1.650	1.605	$1.621(3)^b$

Table 1.3: Properties of the permenent sextupole magnets which reported in [25]. The pole-tip fields B_0^{HAL} are calculated from the Halbach formalism. B_0^{MAF} are the predictions from MAFIA[29] which takes account the typical values of the magnetization of the constituting segments and quadratic extrapolation of the flux dnsity. The measured pole-tip fields B_0^{Mea} in the central plane of the magnets are also listed. ^{a}Magnet with conical opening. The first value denote the radius at the entrance, the second value the radius of the exit aperture. ^{b}The value given is not measured separately, the value given is for magnet 5.

Cartesian coordinates using complex numbers, $z = x + iy = re^{i\phi}$, the field inside the magnet bore at a distance r from the central axis is given by the Halbach fomulas[19]:

$$\vec{B}(z) = J \sum_{i=0}^{\infty} \left(\frac{z}{r_1}\right)^{n-1} H_n K_n \tag{1.19}$$

$$n = N + iM \tag{1.20}$$

$$H_n = \frac{n}{n-1}\left[1 - \left(\frac{r_1}{r_2}\right)^{n-1}\right] \tag{1.21}$$

$$K_n = \frac{\sin{(n+1)\epsilon\pi/M}}{(n+1)\pi/M} \tag{1.22}$$

Here the radii r_1 and r_2 correspond to the inner and outer boundaries of the magnet, respectively, and J is the remanent magnetization of the material. The filling factor ϵ, which accounts for slits between the segments required for glueing, is close to 1. From the above set of equations one can derive the radial and tangential components of the magnetic field as a function of r and ϕ in cylindrical coordinates:

$$B_{rad}(r,\phi) = J \sum_{i=0} \infty \left(\frac{r}{r_1}\right)^{n-1} H_n \cos n\phi K_n \tag{1.23}$$

$$B_{tan}(r,\phi) = J \sum_{i=0} \infty \left(\frac{r}{r_1}\right)^{n-1} H_n \sin n\phi K_n \tag{1.24}$$

The pole tip field B_0 of an ideal sextupole magnet given in Eqn. 1.16 is related to quantities in the Halbach formalism by:

$$B_0 = JH_3K_3 \tag{1.25}$$

Tab. 1.3 lists the properties of the newly reported permanent sextupole magnet system[25], which may represent the most advanced permanent sextupole magnet technology.

Magnet	Length(mm)	Inner radius(mm)	$B_0^{MER}(T)$
1	45	7/11	3.2/3.7
2	90	12.5/18	2.5/3.6
3	75	22	4.6
4	70	22	4.6
5	125	22	4.6

Table 1.4: Properties of the SC sextupole magnets which reported in [23]. B_0^{MER} are the predictions from MERMAID[30].

1.3.2 Superconducting Sextupole Magnet

The vanishing electrical resistance of superconducting coils as well as their ability to provide magnetic fields far beyond those of saturated iron is the main motivation for using superconducting magnets. Superconductivity - the infinitely high conductivity below a 'critical temperature' T_c - is observed in a large variety of material but, remarkably, not in some of the best normal conductors like copper, silver and gold, except at very high pressures. Superconducting magnets would profit from a superconductor of as high as a critical temperature as possible. As technological difficulties have up tp now prevented the usage of the ceramic high-T_c conductors, helium cooled niobium and its alloys are still the best choice. The most common superconductor used in magnets is niobium-titanium alloy. $NbTi$ magnets are limited to about $6.5T$ at a helium temperature of $4.4K$(pressurized normal helium) and about $8.5K$ at $2K$(superfluid helium).

In the commonly used sextupole electromagnets, the saturation in the mild iron pole pieces limits pole tip magnetic field to about $0.9T$. The use of permanent magnets is limited by the demagnetization of the material. Substantial increase of the magnetic field might be obtained in a superconducting magnet. At the same time the cold surfaces of the wall of the magnet might be used as a cryopump to get good vacuum conditions along the beam axis. The attraction to use superconducting magnets with high magnetic fields for the atomic beam sources has been discussed many times[28], and the most recent application is reported in [23], in which a $4.8T$ pole tip magnetic field with an magnet aperture of $44mm$ has been constructed for a internal polarized target ABS at the VEPP-3 electron storage ring in Novosibirsk. The properties of these SC sextupole magnets are listed in Tab. 1.4.

1.3.3 The Stern-Gerlach Force of Sextupole Magnets

The stern-gerlach force[17] results from the magnetic moment coupling with external magnetic field, which can be seen from Eqn. 1.1. The lagrange function $\mathcal{L}$ for an atom in hyperfine state $|\,i\,\rangle$ is given by:

$$\mathcal{L} = \frac{m}{2}\left(\dot{x}^2 + \dot{y}^2 + \dot{z}^2\right) - \mu_{|\,i\,\rangle} \cdot \left|\vec{B}\right| \tag{1.26}$$

The absolute value of the magnetic field inside a sextupole magnet, which is aligned along the z-axis, is given by Eqn. 1.16. The magnetic moment $\mu_{|\,a\,\rangle}$ of hyperfine

Hydrogen	Deuterium
$\mu_1^H = \frac{dE_1}{dB} = \frac{1}{2} g_S \mu_B$	$\mu_1^D = \frac{dE_1}{dB} = \frac{1}{2} g_S \mu_B$
$\mu_2^H = \frac{dE_2}{dB} = \frac{1}{2} g_S \mu_B \cos 2\theta$	$\mu_2^D = \frac{dE_2}{dB} = \frac{1}{2} g_S \mu_B \cos 2\theta_+$
$\mu_3^H = \frac{dE_3}{dB} = -\frac{1}{2} g_S \mu_B$	$\mu_3^D = \frac{dE_3}{dB} = \frac{1}{2} g_S \mu_B \cos 2\theta_-$
$\mu_4^H = \frac{dE_4}{dB} = -\frac{1}{2} g_S \mu_B \cos 2\theta$	$\mu_4^D = \frac{dE_4}{dB} = \frac{1}{2} g_S \mu_B$
	$\mu_5^D = \frac{dE_5}{dB} = \frac{1}{2} g_S \mu_B \cos 2\theta_-$
	$\mu_6^D = \frac{dE_6}{dB} = \frac{1}{2} g_S \mu_B \cos 2\theta_+$

Table 1.5: Magnetic moments of the hyperfine states for hydrogen and deuterium. The formulas have been used with $\epsilon \simeq 0$

state $|\, i\,\rangle$ equals the sum of the magnetic moments of the electrons and the nucleons. The resulting equations of motion are then given by:

$$\begin{aligned} \ddot{r} &= \frac{r_0^4 \dot{\phi}_0^2}{r^3} - sgn(\mu_{|\,i\,\rangle}) \frac{\mu_B B_{pt}}{r_{pt}^2} r \\ \ddot{\phi} &= 0 \\ \ddot{z} &= 0 \end{aligned} \tag{1.27}$$

The magnetic moments for different states of hydrogen and deuterium atoms are listed in Tab. 1.5. The pure states have a constant magnetic moment, while the moments of the mixed states depend on the mixing angles. Atoms in state $\mu_{|\,1\,\rangle}$ oscillate harmonically around the axis of the sextupole magnet in both co-ordinates x and y. A calculation of the frequency of the oscillation yields:

$$\omega^2 = \frac{E_{HFS}}{m\, r_{pt}^2} \frac{B_{pt}}{B_C} = \frac{g_s \mu_B B_{pt}}{m\, r_{pt}^2} \tag{1.28}$$

As $\ddot{z} = \dot{v_z} = 0$, the time can be replaced by the axial co-ordinate z by $t = z/v_z$. Thus the solution of Eqn. 1.27 is:

$$\begin{aligned} r_1(z) &= \sqrt{\frac{1}{2} r_0^2 + \frac{1}{2\omega^2} \left(\dot{r}_0^2 + r_0^2 \dot{\phi}_0^2 \right) + A \cos\left(2kz + \delta_0\right)} \\ A &= \frac{1}{2\omega^2} \sqrt{\dot{r}_0^4 + r_0^4 \dot{\phi}_0^4 + \omega^4 r_0^4 + 2(\omega^2 + \dot{\phi}_0^2) r_0^2 \dot{r}_0^2 - 2\omega^2 \dot{\phi}_0^2 r_0^4} \\ k_1 &= \frac{\omega}{v_z} \end{aligned} \tag{1.29}$$

in which x_0 are the value when $t = 0$. The solution for atoms in state $|\,3\,\rangle$ ($|\,4\,\rangle$ in case of deuterium) is given by:

$$\begin{aligned} r_3(z) &= \sqrt{\frac{1}{2} r_0^2 - \frac{1}{2\omega^2} \left(\dot{r}_0^2 + r_0^2 \dot{\phi}_0^2 \right) + A \cosh\left(2kz + \delta_0\right)} \\ A &= \frac{1}{2\omega^2} \sqrt{\dot{r}_0^4 + r_0^4 \dot{\phi}_0^4 + \omega^4 r_0^4 + 2(\omega^2 + \dot{\phi}_0^2) r_0^2 \dot{r}_0^2 + 6\omega^2 \dot{\phi}_0^2 r_0^4} \\ k_3 &= \frac{\omega}{v_z} \end{aligned} \tag{1.30}$$

The solutions indicate that the state $|\,3\,\rangle$ are defocused. If the atom is injected into the sextupole magnet without angular momentum ($\dot{\phi}_0 = 0$), The solutions are an cos ocillation for the state $|\,1\,\rangle$ or an exponential increase of the radius for the state

$|3\rangle$. The wavelength stays constant independently of the angular momentum. The solutions for the mixed states can be calculated numerically using a Runge-Kutta method[18]. They show a similar behavior in some distance to the sextupole axis, where $B(r) \geq B_C$ and therefore $\cos 2\theta \simeq 1$, whereas their behavior differs close to the sextupole axis[13]. In case of deuterium, where the critical field B_C is only about $11.7mT$, the difference between the pure and the mixed states is less pronounced compared to hydrogen.

In the ABS with sextupole magnet systems, the defocused atoms hit either the inner walls of the sextupoles or the vacuum chambers and are pumped away. Only atoms with $m_S = +\frac{1}{2}$ of a matching velocity are able to transmit the system. The atomic beam which leaves the sextupole system is - in high holding field - nearly 100% electron polarized. Fig. 1.10 shows the result of a trajectory calculation using a tracking program[18] for the HERMES ABS.

1.4 Target Polarization — recombination and molecular flow in long tubes

The average polarization P^T of nucleons in the target can be described by the following equation:

$$P^T = \alpha_0 \cdot [\alpha_r + (1 - \alpha_r) \cdot \beta] \cdot P_a \tag{1.31}$$

in which α_0 is the initial atomic fraction which is injected by the ABS into the cell, α_r is the fraction of the injected atoms which survive the recombination in the cell, $1 - \alpha_r$ is the fraction of the injected atoms which recombine to molecules, the molecules coming from recombination still reserve some polarization which is measured by the factor β[14], P_a is the polarization of the target atoms. To know the nuclear spin polarization of the target which seen by the HERA positron beam, it

[13] The difference is not large, as the sextupole force is weak in low field

[14] A detailed analysis of HERMES measurements limits its possible range for hydrogen to $0.2 \leq \beta \geq 1$[31]

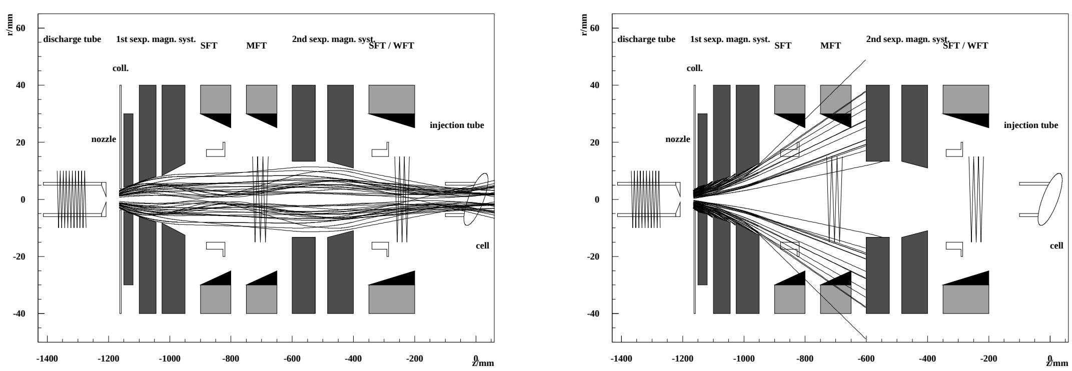

Figure 1.10: Trajectories of Hydrogen Atoms in the Sextupole System of the HERMES ABS, calculated by a MC simulation[18]. Left: Focused pure hyperfine state $|1\rangle$. Right: Defocused pure hyperfine state $|3\rangle$ (state $|4\rangle$ for deuterium).

is important[15] to know the recombinated molecular fraction of the target[32] as well as the sampling corrections[35] because only a sample of the target gas is measured.

1.4.1 Recombination

Because of the low densities of the HERMES target, volume recombination can be neglected. Hydrogen/Deuterium atoms will only recombine by surface catalytic processes. It is found that the temperature and gas density dependance of surface recombination can be consistently described by a combination of three mechanisms[32]. The first one, dominating at temperature above $120K$, is an activated Eley-Rideal reaction. The second process dominating below $100K$ in case of new storage cells is interpreted as a tunnelling reaction between a physically absorbed state and a chemically bond atom of the surface. When the storage cell coating is aged by the influence of the HERA positron beam the second process is suppressed and the third (weak) process starts to dominate, which is described by Langmuir-Hinshelwood type reactions between physically absorbed atoms.

The Langmuir-Hinshelwood (L-H) process, where two absorbed atoms or molecules react with each other and the Eley-Rideal (E-R) process in which an atom or molecule impinging on the surface from the gas phase reacts directly with an absorbed atom or molecule. Typically both reaction types were investigated by surface science using chemically absorbed atoms or molecules on metal surfaces. The typical binding energy of chemical absorption is above $1eV$ and chemically absorbed atoms can not evaporate at room temperature. Physical absorption is caused by the relatively weak Van-der-Waals interaction with typical binding energies between $0.01eV$ and $0.1eV$. Physical absorbed atoms stay only for short time intervals (less than *nanoseconds*) at room temperature on the surface before they evaporate back into the gas phase. A proper Drifilm coating is a surface without chemical absorption sites, as it is chemically saturated and has ideally no unpaired electrons. A schematic diagram of a proper Drifilm coating is shown in 1.11. One can describe the hydrogen atoms of the CH_3-groups of the Drifilm coating, that are ideally building the surface, in terms of chemissorption. A Drifilm coating can then be understood as a surface with a saturated monolayer of chemical absorbed hydrogens.

It has been observed sometimes that accidental losses of the HERA positron beam coincide with a sudden decrease of the measured atomic fraction α_r^{TGA}[31][13]. The presence of water is important since water is known to inhibit hydrogen/deuterium recombination as the chemical binding energy of a hydrogen atom in water ($5.16eV$)

[15]For details, please refer to [13] and [56].

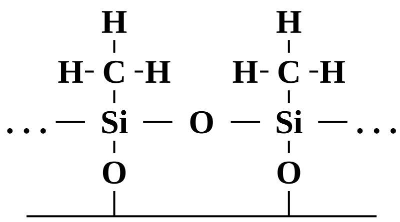

Figure 1.11: Schematic diagram of a proper Drifilm coating[34]. Possible chemical structures of misformed coatings are discussed in the same references. Proper Drifilm coatings are hydrophobic.

is larger than in a hydrogen molecule ($4.52eV$). The bond strength of a hydrogen atom in a methyl group of Drifilm is assumed to be close to the bond strength of $H - CH_2Si(CH_3)_3$ which is $4.3eV$. The reaction of a hydrogen atom with Drifilm $H + a - CH_3 \rightarrow H_2 + a - CH_2 + Q$ is exothermic while $H + H_2O + Q \rightarrow H_2 + OH$ is endothermic and suppressed at low temperatures. It is assumed that the first process is quickly followed by the process $H + a - CH_2 \rightarrow a - CH_3 + Q$ so that the coverage of these sites by hydrogen is close to unity.

The measurememt[32] lead to the conclusion that "***recombination between physical absorbed atoms is negligible at the typical target operation temperatures between*** $60K$ ***and*** $100K$***. Hence recombination at the working point is independent of the gas density since the coverage of the chemically absorbed layer is close to unity***".

1.4.2 Molecular Flow in Long Tubes

Gas diffusion in the low pressure regime is called *molecular flow*. According to Fick's First Law the gas flow Φ along the axis of a long tube is proportional to the gradient of the pressure:

$$\Phi = -DS\frac{\partial p}{\partial z} \tag{1.32}$$

where S is the cross-section of the tube and D the diffusion constant[36]. Particle flow fulfills the continuity equation:

$$\dot{n} + \nabla \cdot \vec{j} = q \tag{1.33}$$

where the n is the particle density, $\vec{j}$ is the particle flux density and for a one-dimension flow is the Φ of Eqn. 1.32, q is the particle source density. Combine Eqn. 1.32 and 1.33 for one dimension flow to:

$$\dot{n} - \frac{\partial D}{\partial z} \cdot \frac{\partial n}{\partial z} - D\frac{\partial^2 n}{\partial z^2} = q \tag{1.34}$$

In case of tubes with constant cross-section and temperature, the gradient of the diffusion constant D vanishes and one finds the $diffusionequaiton$:

$$\dot{n} = D\frac{\partial^2 n}{\partial z^2} + q \tag{1.35}$$

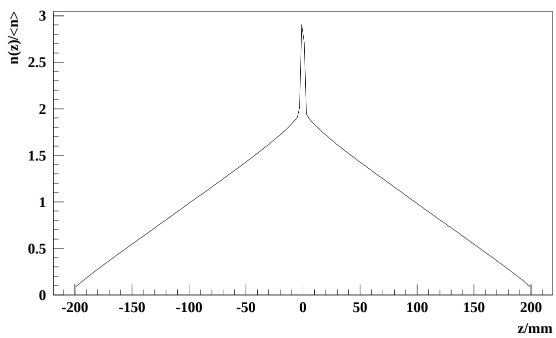

Figure 1.12: Density profile of atoms in the HERMES storage cell is shown in Fig. 1.12. The peak above the trianglar density distribution corresonds to the injected atomic jet. The density is only close to zero at the edge of the storage cell. The distribution was produced by a molecular flow Monte Carlo simulation[38].

In case of a steady flow and in absence of source, the solution of this equation for a tube of L, which fulfills the boundary conditions $n(0) = n_0$ and $n(L) = 0$, is[16]:

$$n(z) = n_0 \left(1 - \frac{|z|}{z}\right) \tag{1.36}$$

This solution is valid for $|z| < L$ and implies a source in form of a Dirac-δ-function at $z = 0$, which represents the injection by the ABS. Density profile of atoms in the HERMES storage cell is shown in Fig. 1.12. The peak above the trianglar density distribution corresonds to the injected atomic jet. The density is only close to zero at the edge of the storage cell. The distribution was produced by a molecular flow Monte Carlo simulation[38].

[16]The condition $n(L) = 0$ is an approximation for long tubes and negligible background pressures.

Chapter 2

Experiment Setup

The HERMES hydrogen/deuterium target has been running since 1996. It uses an *Atomic Beam Source* to generate nuclear-spin polarized hydrogen/deuterium atomic beams. The atomic beams are injected into the target storage cell which locate within the HERA positron storage ring. A magnet surrounding the storage cell provides a holding field which defines the polarization direction and also prevent the spin depolarization process. A sample of target gas are analyzed by an so-called *Target Gas Analyzer* to get the target composition. The polarization of the hydrogen/deuterium target is measured by a *Breit-Rabi Polarimeter*. A schematic view of the whole target setup is given in figure 2.1 in which the magnet coils was used in 1996-2000 to produce a longitudinal polarized target.

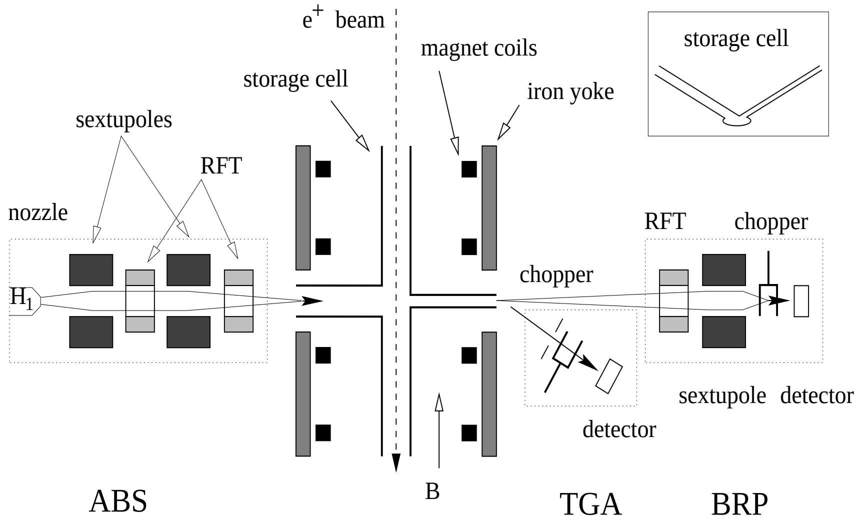

Figure 2.1: Schematic view of the HERMES internal polarized gaseous target. The magnet coils was used in 1996-2000 to produce longitudinal polarized target.

2.1 The Atomic Beam Source

The setup of the HERMES ABS[39] is shown in Fig. 2.2. Hydrogen/Deutrium molecules are dissociated via electron impact provided by a radio frequency(microwave for deuterium) dissociator. The dissociated atoms expand through a helium-cooled nozzle which is cooled down at $100K$. By using a skimmer and a collimator a high

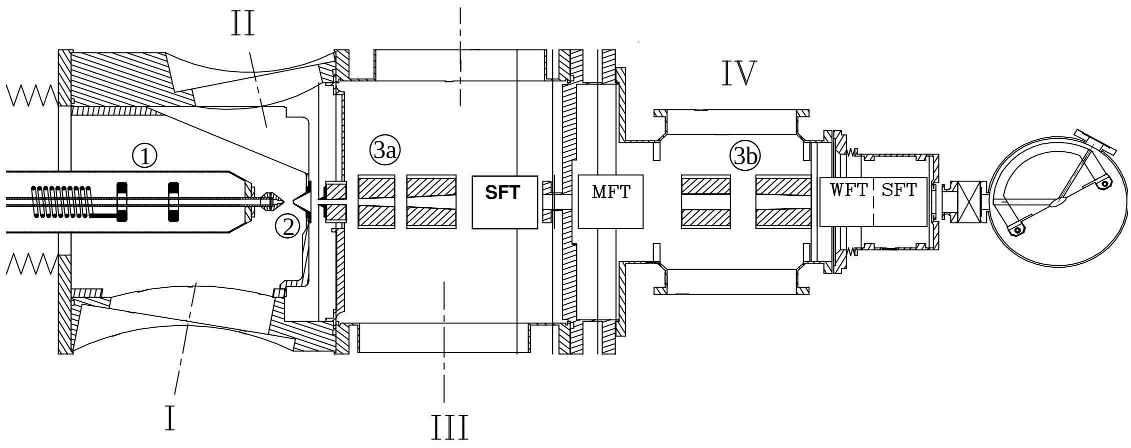

Figure 2.2: schematic view of the ABS on the HERMES target.In which (1) represents the RF dissociator, (2) is the beam formatting parts including a nozzle, a skimmer and a collimator, (3a) and (3b) are the two sets of sextupole magnets . The axis of the ABS is titled by $30°$ downwards with respect to the horizontal plane (A-A). I to IV represent differential pump stages (see also Tab. A.3. MFT between the two sextupole magnet systems is retuned as a WFT for the Hydrogen running. SFT/WFT in the appendix can be used separately but not in the same time.).

intensity beam is formed. The geometry parameters of the beam formation pieces which listed in Tab. A.2 are chosen to match the divergence of the beam within the acceptance of the the sextupole magnet system. These sextupole magnets focus atoms with positive electron spin and deflect atoms with negative electron spin away from the atomic beam axis. A spin polarized beam of hydrogen (deuterium) atoms with approximately $6.4 \times 10^{16} s^{-1}$ ($5.2 \times 10^{16} s^{-1}$) is achieved by the HERMES target ABS.

By exchanging the hyperfine state populations using high frequency transitions (HFT), nucleon spin polarization is achieved. For the normal operation of the hydrogen target, only the HFT units in the appendix are used. SFT/WFT in the appendix can be used separately but not in the same time. In case of deuterium, the transition units between the two sextupole subsystems are also used. MFT between the two sextupole magnet systems is retuned as a WFT for the hydrogen target. In the Beam Loss Measurement[40], only the two HFTs between the two sextupole subsystems are used. The schematic view of the HFT setup are plotted in Fig. 2.3. The injection modes which is available in the HERMES ABS are listed Tab. 2.1. The MFT(WFT) transitions are generated by a coil that is feed by a high frequency emitter and an amplifier. A static magnetic field with perpendicular orientation and a gradient that increase along the direction of the atomic beam is superimposed. The SFT transitions are generated by a band conductivity resonator[41]. The high frequency is coupled to one of the two resonator rods. The second rod is excited into oscillations by the HF field. The resonator for the hydrogen transitions was operated at $1425MHz$ and $419MHz$ for deuterium respectively. The development of resonators with rods tilted[42] relative to the axis of the atomic beam, and thus to the static field, has come to the application that use a single band conductivity resonator as both a MFT and a SFT which is shown in the ABS appendix.

A description of the hyperfine transition principle is available in Sec. 1.1 and 1.2. The effect of an adiabatic hyperfine transition on the hyperfine population can be represented by a matrix as described in Eqn. 1.8 or 1.9. For hydrogen, the populations of different states injected into the storage cell per unit time ($I_{|i\rangle}$ in state $|i\rangle$) are given by:

$$\begin{pmatrix} I_{|1\rangle} \\ I_{|2\rangle} \\ I_{|3\rangle} \\ I_{|4\rangle} \end{pmatrix} = T^{Appendix}_{SFT/WFT} \cdot (\sigma_{ij}) \cdot T_{MFT} \cdot T_{SFT} \cdot \begin{pmatrix} 1 \\ 1 \\ 1 \\ 1 \end{pmatrix} \tag{2.1}$$

in which $T^{Appendix}_{SFT/WFT}$ is the transition matrix for the SFT/WFT in the appendix, T_{SFT} and T_{MFT} (T_{WFT} for hydrogen) is the transition matrix for the SFT and MFT (WFT for hydrogen) respectively between the two sextupole subsystems, (σ_{ij}) is the transmission probability matrix, which enters the first sextupole subsystem in state $|i\rangle$ and the second in state $|b\rangle$. In case that the HFT unit is not working, the transition matrix for it is a unit matrix. For example if only the SFT 2-4 transition between the two sextupole magnet is working, the transmission can be described in the following way:

$$\begin{pmatrix} 1 \\ 1 \\ 1 \\ 1 \end{pmatrix} \overset{1.sexp.}{\rightarrow} \begin{pmatrix} \sigma_1 \\ \sigma_2 \\ \sigma_3 \\ \sigma_4 \end{pmatrix} \overset{SFT2-4}{\rightarrow} \begin{pmatrix} \sigma_1 \\ \sigma_2(1-\epsilon_{24}) + \sigma_4\epsilon_{24} \\ \sigma_3 \\ \sigma_2\epsilon_{24} + \sigma_4(1-\epsilon_{24}) \end{pmatrix} \overset{2.sexp.}{\rightarrow} \begin{pmatrix} \sigma_{11} \\ \sigma_{22}(1-\epsilon_{24}) + \sigma_{42}\epsilon_{24} \\ \sigma_{33} \\ \sigma_{24}\epsilon_{24} + \sigma_{44}(1-\epsilon_{24}) \end{pmatrix} \tag{2.2}$$

The sextupole system is optimized for highest initial polarization and intensity in case of hydrogen running. As the HFT units in the appendix are used in the normal running, the initial polarization depends dominantly on the efficiencies of these HFT units and the target holding field. As the transmission probabilities of the HERMES ABS are nearly ideal in this case ($\sigma_{11} \simeq \sigma_{22} \simeq 0.45$ and $\sigma_{33} \simeq \sigma_{44} \simeq 0$)[18], the

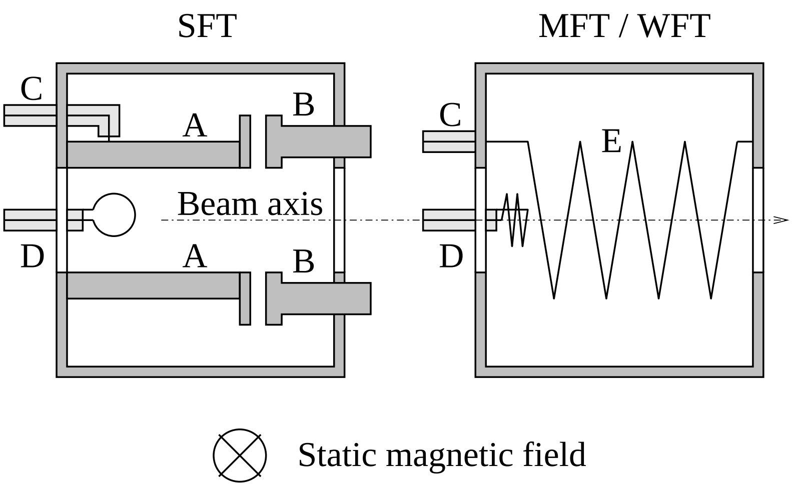

Figure 2.3: Schematic View of HFT units setup in the HERMES target. The different components are the resonator rods (A), the adjustable capacitor (B), the coaxial RF power input (C), the pick-up loop (D) and the RF coil (E).

initial hyperfine population is given by:

$$P_{z+} \; : \; \frac{1}{2}\begin{pmatrix} 1 \\ 1-\epsilon_{24} \\ 0 \\ \epsilon_{24} \end{pmatrix} \qquad\qquad P_{z-} \; : \; \frac{1}{2}\begin{pmatrix} 1-\epsilon_{13} \\ 1 \\ \epsilon_{13} \\ 0 \end{pmatrix} \tag{2.3}$$

The transmission propapability matrix is estimated by a MC simulation[18] and the results are listed in Tab. 2.2. In case of deuterium, the result of this calculation predicts no significant dependence on m_I of the transmission. It is therefore sufficient to describe the ABS transmissions for Deuterium by $\sigma_{\uparrow\uparrow}$, $\sigma_{\downarrow\downarrow}$, $\sigma_{\uparrow\downarrow}$ and $\sigma_{\downarrow\uparrow}$, where the arrows refer to the electron spin. It was found that the setup of the individual

Gas	HFT (betw. 6-poles)	HFT (app.)	Inj. States	P_e	P_z	P_{zz}	Use
	-	-	$\|1\rangle, \|2\rangle$	+1	0	-	Cal
H	-	WFT 1-3	$\|2\rangle, \|3\rangle$	0	-1	-	Data
	-	SFT 2-4	$\|1\rangle, \|4\rangle$	0	+1	-	Data
	SFT 2-4 / MFT 2-3	-	$\|1\rangle$	+1	+1	-	Cal
	WFT 1-3 / MFT 1-3	-	$\|2\rangle$	+1	-1	-	Cal
	SFT 2-4 / MFT 2-3	WFT 1-3	$\|3\rangle$	-1	-1	-	Cal
	WFT 1-3 / MFT 1-3	SFT 2-4	$\|4\rangle$	-1	+1	-	Cal
	WFT 1-3, SFT 2-4	-	none	-	-	-	Cal
	-	-	$\|1\rangle\ \|2\rangle\ \|3\rangle$	+1	0	0	Cal
D	SFT 2-5	WFT 1-4	$\|3\rangle\ \|4\rangle$	0	-1	+1	Data
	SFT 3-5	SFT 2-6	$\|1\rangle\ \|6\rangle$	0	+1	+1	Data
	MFT 1-4	SFT 3-5	$\|2\rangle\ \|5\rangle$	0	0	-2	Data
	MFT 1-4	SFT 2-6	$\|3\rangle\ \|6\rangle$	0	0	+1	Data
	MFT 3-4, SFT 2-6	-	$\|1\rangle$	+1	+1	+1	Cal
	WFT 1-4, SFT 2-6	-	$\|2\rangle$	+1	0	-2	Cal
	WFT 1-4, SFT 3-5	-	$\|3\rangle$	+1	-1	+1	Cal
	MFT 3-4, SFT 2-6	WFT 1-4	$\|4\rangle$	-1	-1	+1	Cal
	WFT 1-4, SFT 3-5	SFT 3-5	$\|5\rangle$	+1	0	-2	Cal
	WFT 1-4, SFT 2-6	SFT 2-6	$\|6\rangle$	-1	+1	+1	Cal

Table 2.1: Injection modes of the atomic beam source. The table shows the high frequency transition units employed (2^{nd} and 3^{rd} column), the injected hyperfine states and the resulting electron (P_e), nuclear (P_z) and tensor (P_{zz}) polarizations in the ideal case of unitary efficiencies of sextupole system and transition units and no depolarization inside the target cell. The last column clarifies the purpose of each mode (Cal: calibration, monitoring; Data: HERMES data taking). For some injection mode (i.e. the hydrogen no state and some deuterium single states [13]) The MFT between the sextupoles has to be tuned as a WFT 1-4. The no state injection mode is possible only for the hydrogen case and it is operational since April 2002.

State	$\|1\rangle$	$\|2\rangle$	$\|3\rangle$	$\|4\rangle$
$\|1\rangle$	0.45	0.45	0.033	0.047
$\|2\rangle$	0.45	0.45	0.03	0.043
$\|3\rangle$	0.009	0.0085	0	0
$\|4\rangle$	0.013	0.013	0	0

State	$\uparrow$	$\downarrow$
$\uparrow$	0.45	0.035
$\downarrow$	0.009	0.0

Table 2.2: Absolute transmission probabilities σ_{ab} of the ABS sextupole system calculated by a tracking program for hydrogen (left table) and deuterium (right table) at the working point of the ABS. The number of the row refers to the hyperfine state in the first subsystem and the number of the column to the state in the second subsystem. The relative transmitted intensity of the rejected state of the nuclear polarized states of deuterium is $0.035/0.45 \simeq 7.8\%$. For the discussion of the injected polarization, one can use the relative transmissions, which are defined by $\sigma_{ab} = \sigma_{ab}^{abs}/\sigma_{11}$. Due to the low critical field $B_C^D = 11.68\,mT$ of Deuterium, the transmissions probabilities depend only on the value of m_S. $\sigma_{\uparrow\downarrow}$ is the transmission probability for an atom, which is in state $m_S = \frac{1}{2}$ in the first sextupole subsystem and in state $m_S = -\frac{1}{2}$ in the second.

transitions is less robust in case of deuterium, which is related to the low required field values for the MFT/WFT transitions. An additional problem is the location of the transitions units within the ABS. The small distance of the SFT unit to the first sextupole subsystem leads to an influence of the fringe fields of the sextupole magnets on the transition setup.

2.2 The Target Cell and the Target Magnet

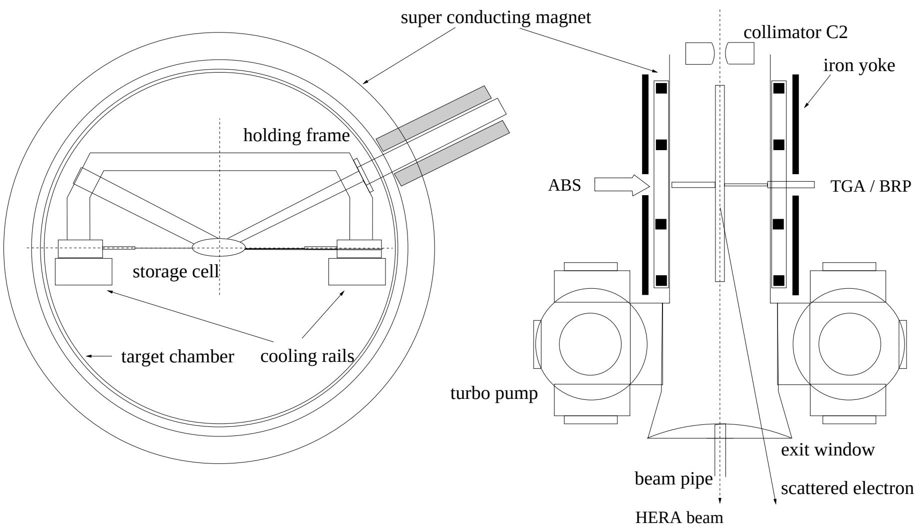

Figure 2.4: Schematic View of the Superconductive Longitudinal Magnet along the HERA beam direction (left) and from the top (right)

A necessary requirement for the HERMES experiment is a sufficient luminosity which depends on the target density. With a gas jet target the surface densities achieved were $2 \times 10^{11} cm^{-2}$[43]. A new technique was suggested and tested which a storage cell tube is used. In the HERMES experiment, the target density is increased by more than two orders of magnitude by injecting the particle beam into a T-shape storage cell. The polarized atoms will collide with the cell surface for hundreds of times before they flow out of the cell.

The HERMES target storage cell[33] consists of an elliptical beam tube made from $75\mu m$ pure aluminum sheets. The surface of the cell is coated with Drifilm[34] to decrease the recombination on the surface. The beam tube of the cell has a cross-section of $8.9mm \times 21mm$ and a length of $40cm$ for 2002 running. The positron beam goes through the cell which is electrically connected to the HERA positron beam pipe by wake field suppressors, which are made of copper and designed to guide the electromagnetic field of the bunched HERA positron beam. The storage cell is mounted on cooling rails whose temperature is controlled by the help of gaseous Helium as well as a controlling heater. The temperature of the cell is monitored by three temperature sensors during the running and the cell is working under a temperature of $100K$ which is found optimal for the minimal wall recombination and wall depolarization[1].

The ABS injected polarized Hydrogen/Deuterium atoms into the storage cell through an injection tube which is $10cm$ long with a diameter of $10mm$. The target gas flows out of the cell tube from the open ends into the scattering vacuum chamber. Parts of the target gas are sampled through a $10cm$ long sample tube with a $5mm$ diameter which is extended by a $10mm$ diameter extension tube with $10cm$ length towards the measuring devices. Both injection tube and sample tube are mounted at an angle of $30°$ respect to the horizontal plane. The target cell is installed in the scattering chamber which is kept in ultrahigh vacuum around $2 \times 10^{-7} mbar$ for normal polarized running.

The HERMES storage cell is installed in a static holding magnetic field which provides the target spin direction and ensures high spin polarization of the mixed hyperfine states. From 1996 to 2000, the HERMES target was longitudinally polarized by a superconductive solenoid consisting of four coils[31] (Fig. 2.4). For the current running starting from 2001, a transverse magnet was installed instead of the longitudinal magnet for transverse data taking. Due to measurements made with

[1]In 2002 running, the cell has been working under a temperature of $80K$ for higher target density thus higher luminosity for HERMES data taking.

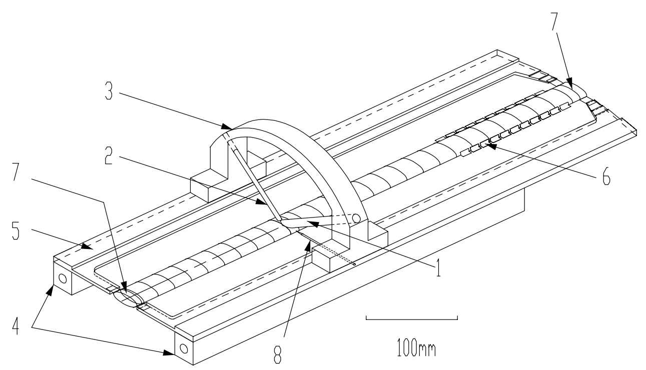

Figure 2.5: The HERMES Storage Cell. Components are: (1) injection tube; (2) Sample Tube; (3)Support Arch; (4) Cryogenic-cooling and Support rails; (5) Support Plates; (6) Cell Extension with pumping apertures; (7) Cell End Support Collars; (8) Unpolarized Gas Feed Capillary.

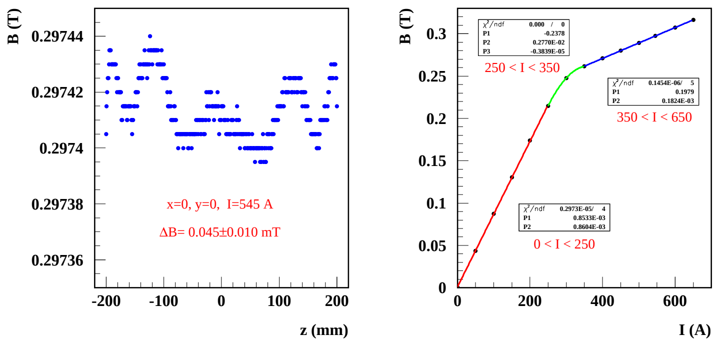

Figure 2.6: [56]The left plot shows the transverse magnetic field uniformity measured along the magnetic axis at the nominal field strength $B = 297mT$. Along the other directions, uniformities of $\Delta B_y = 0.15mT$ and $\Delta B_z = 0.60mT$ have also been measured. On the right plot the relation between magnet current and generated field, measured in the center of the magnet is shown.

the longitudinal magnet and beam-induced depolarization calculations it becomes necessary to achieve a uniformity of $\delta B/B < 1.4 \times 10^{-4}$ under a center field of $0.3T$. To prevent the target magnet from disturbing the HFT units of the target ABS, the stray field along the 30° line is minimized.

The transverse magnetic field has been measured which found that satisfies the design requirements (Fig. 2.6 from [56]). Because of the new beam-induced σ-resonance[2], the beam-induced σ-resonance depolarization has been carefully studied[56]and around 1% σ-resonance depolarization was observed. To improve the uniformity of the holding magnetic field, a new cell with a correction coil is designed by Ferrara group which is planed to install in May 2003(Chp. 4).

2.3 The Unpolarized Gas Feed System

The unpolarized gas feed system is used to inject gas into the storage cell or the target chamber directly. The UGFS system can inject Hydrogen, Nitrogen, Helium and Oxygen. It is used for the HERMES unpolarized physics program and for the target calibrations (Sec. 3.3). The flow is controlled by a flow regulator and a thermovalve. A differential baratron is used to measure the pressure drop caused by the flow resistance of a small capillary (Fig. 2.5) which is proportional to the flow through.

Most recently[46] the UGFS was used to determine the ABS absolute intensity via the HERMES luminosity monitor. By comparing the Luminosity count rates over the HERA positron beam current ($Lumi/Curr$) when the ABS is working with the one when the UGFS is injecting Hydrogen Flows into the celll, the absolute intensity of the ABS is avaible. It is found that the absolute intensity of the ABS is about 15% lower than the value measured before in 1997. It may due to the ABS moving backwards from the cell center by a distance of $3cm$[61] which affects the focusing ability of the ABS sextupole magnet system[3].

[2]Beam-induced depolarizations are distinguished between π-resonance, when the rf-field is perpendicular to the static field, and σ-resonance when the two fields are parallel.

[3]During the HERA shutdown starting from March 2003, it was found that the axis of the ABS

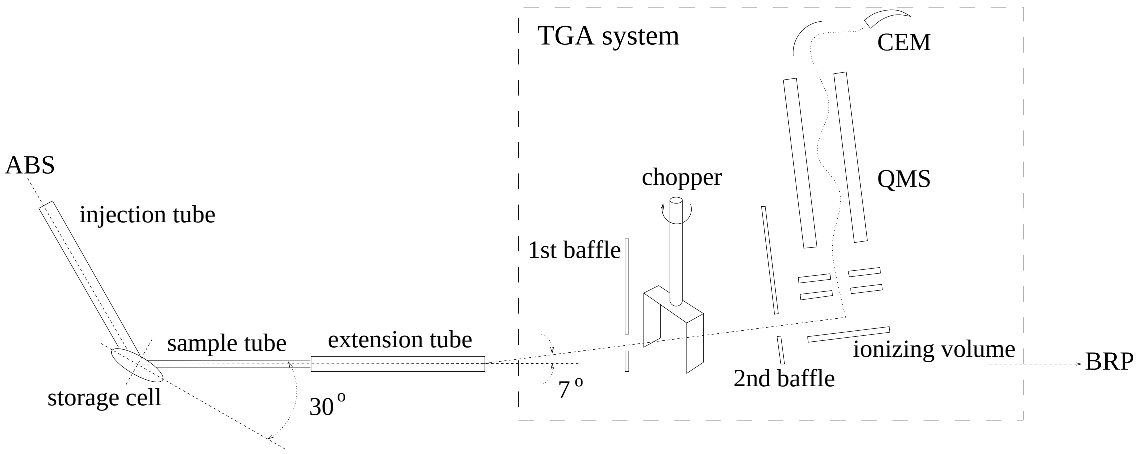

Figure 2.7: Schematic Viw of the HERMES target TGA. The target gas diffuse through the sample tube and the extension tube and is measured by the TGA. A chopper is is used to substract the background rate of the residual gas in the TGA vacuum chamber. The baffles prevent atoms from hitting the inner walls of the cross beam ionizer. The axis of the cross beam ionizer is tilted by 7 relative to the axis of the extension tube.

2.4 The Target Gas Analyzer

The Target Gas Analyzer[44] has been developed to determine the relative amount of atomic and molecular hydrogen/deuterium for the HERMES polarized gaseous target. The TGA is located between the cell chamber and the Breit-Rabi Polarimeter with whom it shares the vacuum system2.8. The vacuum system mainly consists of titanium sublimation pumps and cryo pumps with a total nominal pumping speed of $7000l/s$, and has a typical pressure of $3.5 \times 10^{-9} mbar$ in the chamber during operation.

Fig. 2.7 shows a schematic view of the TGA setup. It consists of a chopper, two baffles, a 90° off-axis quadrupole mass spectrometer (Balzers QMA 430) with a cross beam ionizer and a channel electron multiplier (DeTech 401A) for single ion detection. The chopper rotating at $5.5Hz$ between the two baffles is used to distinguish between particles from the sample beam and those from residual gas. One baffle is mounted in short distance to the extension tube and the other one directly in front of the ionizer volume. The baffles prevent atoms from hitting and recombining on the inner walls of the cross beam ionizer, which could cause a virtual molecular beam signals. The axis of the cross beam ionizer is tilted by 7° relative to the axis of the extension tube. Particles entering the ionizing volume are ionized by $70eV$ electrons emitted from a filament. After being filtered by the quadrupole mass spectrometr the remaining ions are counted by the channeltron and stored in a multichannel time resolving counter with 2048 bins on a digital signal processor (DSP) board. Frequency drifts of the chopper motor are compensated by an adjustment of the bin length by the DSP software and has a typical $175\mu s$ bin length. A time spectrum is shown in Fig. 2.9. A trigger signal from the chopper is used to synchronize the chopper status and the correlated counting rates. The

nozzle is not in the same line with the axis of the collimator.

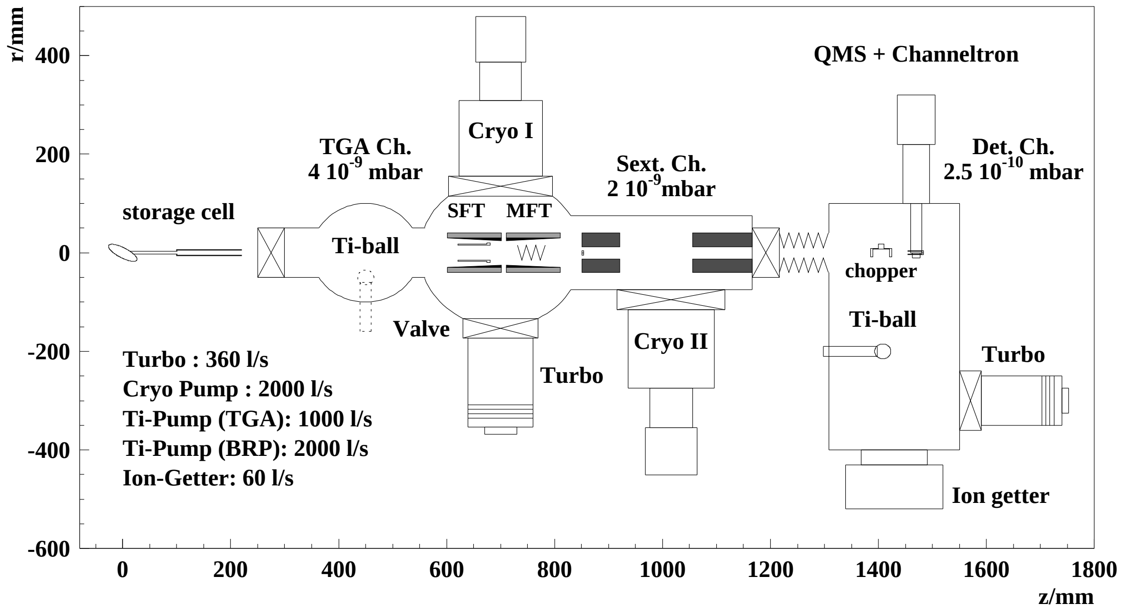

Figure 2.8: Side View of the TGA and BRP Vacuum System.

beam rates are calculated by the difference of the count rates in the periods with open and closed chopper. The counts of $16-32$ chopper periods are summed up for a measurement and the statistical error of the beam rates is estimated by the analysis of the time spectrum[38].

A dead time correction has to be applied when the adsolute count rates are high ($\geq 1MHz$). The emission current of the TGA cross bean ionizer has to be reduced when the background rates exceed $1MHz$, in order to keep the dead time correction small. The beam rates is also corrected for the virtual signals from hydrogen/deuterium molecules as well as water molecules. In case of hydrogen, the beam rates of the masses 1, 2 and 18 $amu.$ have been measured and a net hydrogen beam rate $\tilde{S}$ was calculated by:

$$\tilde{S} = S_1 - k_2 S_2 - k_{18} S_{18} \tag{2.4}$$

the correction constants k_2 and k_{18} were found by the variation of the partial pressures of water and H_2 during a warmup of the cryogenic pumps in the sextupole chamber with open gate valves. The correction scheme has been tested in regular time intervals by closing the valve between BRP(TGA) and target chamber. The net atomic beam rate $\tilde{S}$ has to be zero in this case.

2.4.1 Interpretation of the TGA Beam Rates

The atomic S_a and molecular S_m count rates of the TGA are proportional to the corresponding fluxes Φ_a and Φ_m into the TGA times the ionization cross section σ_a^{ion} (σ_m^{ion})and the detection probability ϵ_a (ϵ_m)[4]:

[4] The detection probabilities ϵ_a (ϵ_m) include the transmission probabilities of the ions through the quadrupole mass spectrometer. Magnetic fringe fields from the target region, caused by the

$$S_{a,m} \propto \Phi_{a,m} \cdot \sigma_{a,m}^{ion} \cdot \epsilon_{a,m} \cdot f\,(B, I_{emis}) \cdot \langle \frac{1}{v_{a,m}} \rangle \tag{2.5}$$

The signal count rates also depend on the particle velocities $\langle \frac{1}{v_a} \rangle$ ($\langle \frac{1}{v_m} \rangle$) as well as the TGA emission current I_{emis}[5] of the electron gun of the cross beam ionizer and the magnetic fringe fields of the target and spectrometer magnet. For the thermalized atoms and molecules one has:

$$\langle \frac{1}{v_m} \rangle = \sqrt{2} \langle \frac{1}{v_a} \rangle \tag{2.6}$$

The total flux of hydrogen/deuterium atoms into the TGA is proportional to the injected flux by the ABS and is given by:

$$\Phi_{TGA} = \Phi_a + 2\Phi_m \propto \Phi_{ABS} \tag{2.7}$$

The partial beam rates S_a and S_m can be interpreted as parts of a total rate:

$$S_{tot} = S_a + \sqrt{2}\kappa S_m \tag{2.8}$$

in which the κ (see Sec. 3.5) is the relative sensitivity of the TGA for the atomic and molecular beam:

$$\kappa = \frac{\sigma_a^{ion} \cdot \epsilon_a}{\sigma_m^{ion} \cdot \epsilon_m} \tag{2.9}$$

As the extension tube (ET) has a higher temperature than the beam tube[6], if one assumes that the beam tube (BT), the injection tube (IT), the sample tube (ST)

HERMES spectrometer magnet and the target magnet have an influence on the trajectories of the ions inside the ionizing volume and the mass spectrometer. During calibration measurements and HERMES data taking periods, the magnets were running stably thus the magnets influence can be taken as the same.

[5]The dependence of the TGA count rates on the emission current is not necessarily linear and not necessarily the same for Atomic count rates and Molecular count rates. Here the assumption that the dependence of the TGA count rates on the emission current for the atomic signals and molecular signals is taken account. See Sec. 3.1

[6]A thermocouple on the extension tube was first installed at the beginning of 1999. In the 1997 analysis, the extension tube temperature has been derived using the expression $T_{ET} = T_0 + \frac{300-T_0}{300}T$, where T_0 is a constant and T is the measured cell temperature[31].

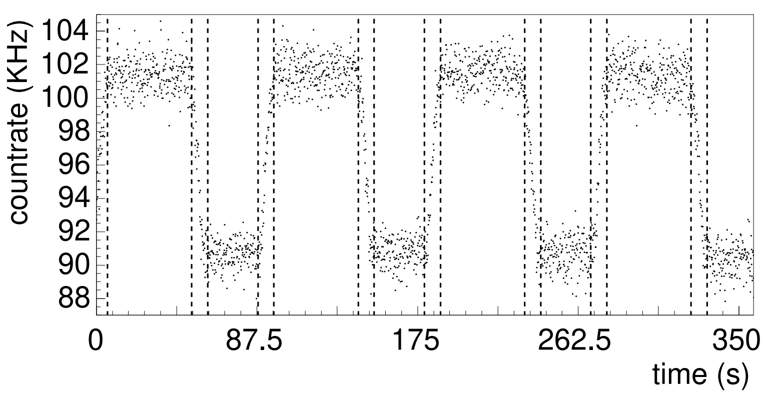

Figure 2.9: A Typical Time spectrum of atomic count rates in the TGA. The vertical lines indicate the bin numbers corresponding to the limits between the chopper positions open, undefined and closed. The bin length is adjustable and typically set to $175\mu s$.

are on the same temperature ($T_{BT} = T_{IT} = T_{ST} = T$), one obtains that:

$$\Phi_{TGA} \propto \Phi_{ABS} \cdot \frac{C_{TGA}}{2C_{BT} + C_{IT} + C_{TGA}} \tag{2.10}$$

where

$$C_{TGA} = \frac{C_{ST}C_{ET}}{C_{ST} + C_{ET}} \tag{2.11}$$

If we express the conductance C_X by $C_X = C_X^0\sqrt{\frac{T_X}{M}}$, in which M denotes the mass of the beam particles, we finds with $2C_{BT} + C_{IT} \gg C_{TGA}$:

$$\Phi_{TGA} \propto \Phi_{ABS} \cdot \frac{1}{1 + \frac{C_{ST}^0}{C_{ET}^0}\sqrt{\frac{T}{T_{ET}}}} \tag{2.12}$$

After using a function $g(T, T_{ET})$ to express the temperature dependence of the count rates resp. the normalized fluxes:

$$\begin{aligned} \phi_a &= \frac{S_a}{g(T, T_{ET}) f(B, I_{emis})} \\ \phi_m &= \frac{\sqrt{2}\kappa \cdot S_m}{g(T, T_{ET}) f(B, I_{emis})} \\ g(T, T_{ET}) &= \frac{1}{g(T_{norm}, T_{ET,norm})} \cdot \frac{C_{ET}^0}{C_{ET}^0\sqrt{T_{ET}} + C_{ST}^0\sqrt{T}} \end{aligned} \tag{2.13}$$

The sum of these flow rates is directly proportional to the ABS injected intensity:

$$\phi_a + \phi_m = \frac{S_a + \sqrt{2}\kappa \cdot S_m}{g(T, T_{ET}) f(B, I_{emis})} = C_{TGA} \cdot \Phi_{ABS} \tag{2.14}$$

so that the TGA is a direct monitor of the ABS intensity. It is convenient to define the TGA-measured dissociation degree α^{TGA} by:

$$\alpha^{TGA} = \frac{\Phi_a}{\Phi_a + \Phi_m} = \frac{S_a}{S_a + \sqrt{2}\kappa \cdot S_m} \tag{2.15}$$

which is independent of the temperature and the emission current[7].

2.4.2 The Initial Atomic Fraction (α_0) and The Fraction of Atoms Surviving Recombination (α_r^{TGA})

The target polarization is calculated by Eqn. 1.31. The initial atomic fraction α_0 is the atomic fraction injected by the ABS. After colliding with the cell, some of the injected atoms will recombine into molecules and the rest of them survive the recombination. The fraction of atoms surviving recombination is defined as α_r.

[7]For the 2002 running, a systematic change of α^{TGA} was observed which coincided with the oxygen ratio in the ABS dissociator, the cell temperature changing, etc., which is not able to explained now[45].

For the atomic fractions which are measured by the TGA, e.g. α_r^{TGA} and α_r^{TGA} respectively, corrections are to be applied which come from MC simulations[56].

The only source of the atomic flux Φ_a into the TGA is the flux of the ABS, however the molecular flux Φ_m has several sources:

- Φ_{ball}—Molecular flux ballistically injected by the ABS:
  As the ABS dissociator has a dissociating efficiency of about 80%, a part of the gas from the dissociator has a fraction of undissociated molecules. This part of molecules are unpolarized and neutralize, so they are not interacted with the sextupole magnets and go straightforward from the nozzle to the injection tube, if one neglects the scattering of the molecules with the other particles within the beam and recombination of the atoms in the ABS. This kind of molecules distribute along the target cell in a triangular shape as shown in Fig. 1.12.

- Φ_{rg}—Molecules diffusing among all the target chamber:
  Because of the infinite pumping speed, there would be molecules diffusing through out of the target chamber which is also existing in the target cell. This kind of molecules distribute along the target cell in a same density everywhere along the cell.

- Φ_r—Molecules recombined in the target cell[8] from the injected atoms:
  This part of molecules are produced by recombination on the cell surface (see Subsec. 1.4.1). This part of molecules are still polarized which is described by the factor β[37]. So far, the lack of information about the molecular polarization has led to apply the conservative value $\beta = 0.5 \pm 0.5$. Recently a set of data taken in 1997 at a warmer cell ($260K$ instead of the normal $100K$) could be used to measure the hydrogen β value with the help of the HERMES spectrometer.

The total molecular flux Φ_m is the sum of the three components:

$$\phi_m = \phi_{ball} + \phi_{rg} + \phi_r \tag{2.16}$$

The fraction of atoms surviving recombination α_r^{TGA} as measured by the TGA is calculated by:

$$\alpha_r^{TGA} = \frac{\phi_a}{\phi_a + \phi_r} \tag{2.17}$$

The initial atomic fraction α_0^{TGA} is calculated by:

$$\alpha_0^{TGA} = \frac{\phi_a + \phi_r}{\phi_a + \phi_r + \phi_{ball} + \phi_{rg}} \tag{2.18}$$

and the atomic fraction measured by the TGA is given by:

$$\alpha^{TGA} = \alpha_0^{TGA} \cdot \alpha_r^{TGA} = \frac{\phi_a}{\phi_a + \phi_r + \phi_{ball} + \phi_{rg}} \tag{2.19}$$

[8] As the extension tube has a much higher temperature ($180K$) than the cell tube and because most of the molecules seen by the TGA come from the extension tube, there is a possibility that a part of the recombined molecules recombine on the surface of the extension tube.

After taking account the different conductance for atoms and molecules, different density contributions inside the target cell, the atomic fraction inside the target cell can be presented by[13]:

$$\alpha_0 = \frac{\phi_a + \phi_r}{\phi_a + \phi_r + (1 + (\sqrt{2} - 1)\alpha_r)(\phi_{ball} + 2\phi_{rg})} \tag{2.20}$$

Calibrations to measure and distinguish the different contributions to the TGA measured molecules signals are presented in Chp. 3, as well as the temperature scan to measure the κ value for the HERMES TGA.

Corrections to get the atomic fractions in the target cell are described precisely in [13] or [56]. This correction takes account of the difference in the number of wall collisions of the atoms within the sample beam and the storage cell and of the possibility of a non-uniform surface in the cell and sample tube with respect to the recombination probabilities per wall collision.

The TGA has been continuously in operation (except for the HERA shutdown periods) at the HERMES target since 1996 and it is found to be a very reliable instrument. For the 2002 polarized hydrogen running, measurements have led to $\alpha_r^{TGA} = (99.5 \pm 0.1)\%$ and $\alpha_0^{TGA} = (95 \pm 3)\%$[45][9].

2.5 The Breit-Rabi Polarimeter

The effective polarization of the HERMES target is obtained by measuring the polarization of a sample of atoms effusing from a sample tube and a extension tube with an atomic beam polarimeter[47]. The design goal of the polarimeter is to precisely measure the relative populations $n_{|i\rangle}$ of the hyperfine states of a thermal atomic hydrogen/deuterium beam of low intensity. The HERMES target polarimeter is of the type so-called Breit-Rabi Polarimeter (BRP)[48]. This kind of

[9]For the 2002 running, the larger error 3% compared with the former years (< 1%) is due to some of unresolved TGA problems. For example, it is found that the TGA atomic count rate distribution of very short periods, in which the ABS should work stable, is in a two Gaussian peak shape. This problem which never seen in the former years is under investigation.

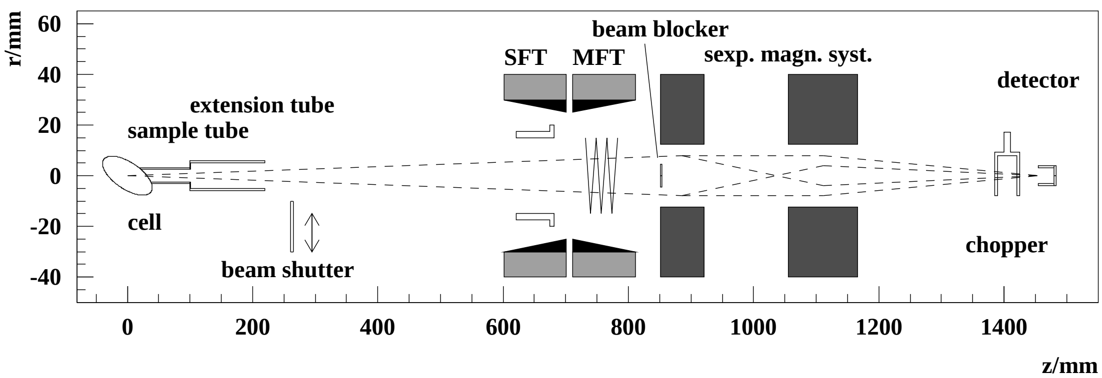

Figure 2.10: Schematic View of the BRP Setup

polarimeter is able to measure the absolute value of the polarization of both nuclei and electrons with a systematic uncertainty of better than 2%. It is also able to allow a measurement to be made in a time period of approximately one minute to be compatible with fast reversal of the target spin direction.

The schematic view of the Breit-Rabi Polarimeter setup is shown in Fig. 2.10 and the side view of the BRP vacuum system is shown in Fig. 2.8. The Breit-Rabi Polarimeter mainly consists of two high frequency transition units (SFT/MFT), a sextupole magnet system and a detector. The hardware geometry parameters are listed in Tab. A.4. The HFT units and the sextupole system are located in the first vacuum chamber, called sextupole chamber, while the detection chamber contains the beam chopper and a detector which is in principle the same with the TGA detector[10]. Both chambers form a differential pumping system with typical residual pressures of $2 \times 10^{-9} mbar$ in the sextupole chamber and $2.5 \times 10^{-10} mbar$ in the detection chamber. The detection chamber and the TGA vacuum chamber are baked out with temperatures of up to $220°C$ after startup.

The sextupole system has been redesigned in order to improve the transmission probability at the working temperature typical of the HERMES target[49]. A 9 mm diameter beam blocker placed in front of the first sextupole magnet ensures that no atoms in the lower energy states can pass through. The SFT unit is realized by a resonator cavity with tilted rods. Two types rf transitions which can be used for both σ and π transitions are possible depending on the orientation of the static field and the rf-field. The resonance frequency of the cavity can change slightly due to thermal drifts, thus it is kept in resonance by a feed back loop using the signal from a pickup coil inside the cavity[18]. The frequency for hydrogen ($1440 MHz$) is different with the one for deuterium ($370 MHz$) and the cavities have to be changed when the atom species is changed. The MFT unit is realized by a solenoid coil. A collins filter is mounted outside the vacuum chamber in order to provide good matching to the rf-source[18]. The MFT unit can be used both for hydrogen ($90 MHz$) and deuterium ($25 MHz$).

2.5.1 Theory of Polarization Measurement

The atomic signals detected by the BRP detector depends on the transmission probabilities of the sextupole system and on the setting of the transition units. The HFT units can be switched on and off, accordingly changing the intensity of the beam reaching the detector:

$$S_i = c \sum_a \left(\sum_b \sigma_b T^i_{ab} \right) I_a \tag{2.21}$$

where σ_a is the probability of atoms in hyperfine state $|\, a\,\rangle$ to pass the sextupole system, I_a is the sample beam intensity of atoms in hyperfine state $|\, a\,\rangle$, the factor c represents the geometrical acceptance and detection efficiency of the quadrople mass spectrometer, the matrix T^i_{ab} describes the exchange of the hyperfine states with transition i switched on. If all the HFT units are switched off, the count rate

[10][13] Both the TGA and the BRP are controlled by the same software and their count rates are registered and evaluated by the same Digital Signal Processor module

in the detector S_{off} is:

$$S_{off} = c \sum_a \sigma_a I_a \tag{2.22}$$

So we can see that the detector count rate is a set of linear functions of the intensity I_a:

$$S_i = c \sum_a M_{ia} I_a \tag{2.23}$$

where M_{ia} is the matrix which depends on the transition efficiencies of the HFT units and the transmission probabilities. For example, in the case of the SFT $1-4$ on, the count rate is given by:

$$\begin{aligned} S_{s14} &= c\{[\sigma_1(1-\epsilon_{s14}) + \sigma_4\epsilon_{s14}]I_1 + \sigma_2 I_2 + \sigma_3 I_3 \\ &+ [\sigma_4(1-\epsilon_{s14}) + \sigma_1\epsilon_{s14}]I_4\} \end{aligned} \tag{2.24}$$

The set of linear equations Eqn. 2.23 can be solved using four different beam rates S_i in case of hydrogen and six in case of deuterium, if the measurement matrix M_{ia} is already available. The intensities I_a are calculated by the inverse matrix $R = M^{-1}$:

$$I_a = c^{-1} \sum_b R_{ab} S_b \tag{2.25}$$

The hyperfine state population numbers n_a of the beam are obtained by a normalization of the calculated intensities:

$$n_a = I_a / \sum_a I_a \tag{2.26}$$

The electron polarization and nuclei polarization can be calculated using the normalized expectation values of the corresponding spin operators. For hydrogen the calculation yields:

$$\begin{aligned} P_e &= n_1 - n_3 + (n_2 - n_4)\cos 2\theta \\ P_z &= n_1 - n_3 - (n_2 - n_4)\cos 2\theta \end{aligned} \tag{2.27}$$

for the deuterium:

$$\begin{aligned} P_e &= n_1 - n_4 + (n_2 - n_6)\cos 2\theta_+ + (n_3 - n_5)\cos 2\theta_- \\ P_z &= n_1 - n_4 + n_6 - n_2 + (n_2 - n_6)\sin\theta_+{}^2 + (n_3 - n_5)\sin\theta_-{}^2 \qquad (2.28) \\ P_{zz} &= n_1 + n_4 - n_2 \cdot \frac{1}{2}(3\cos 2\theta_+ + 1) + n_3 \cdot \frac{1}{2}(3\cos 2\theta_- - 1) \qquad (2.29) \\ &\quad -n_5 \cdot \frac{1}{2}(3\cos 2\theta_- + 1) + n_6 \cdot \frac{1}{2}(3\cos 2\theta_+ - 1) \end{aligned}$$

in which mixing angles θ and $\theta_\pm$ are functions of the holding magnetic field B defined by equations listed in Tab. 1.1.

2.5.2 Total Intensity of the BRP

The total intensity of the BRP is defined as:

$$I_{tot} = \sum_a I_a \tag{2.30}$$

There are several reasons[13] for an investigation of the total intensity of the BRP: First, the knowledge of I_{tot} in dependence of the cell temperature allows to compare the atomic flux into the BRP with the corresponding flux into the TGA. It is shown that in [13], that this comparison can be used to investigate the recombination probability of sample and extension tube, which helps to limit the sampling correction. Second, a high value of I_{tot} is required to minimize the statistical uncertainty of the polarization measurement. Third, the knowledge of the velocity distribution of the atoms passing the BRP sextupole system is required for the interpretation of the diffusion time measurements, which is also presented in [13].

There is another very important reason that one would like to investigate the total intensity of the BRP I_{tot}^{BRP}. From the study of [32], "***Recombination between physical absorbed atoms is negligible at the typical target operation temperatures between*** $60K$ ***and*** $100K$***. Hence recombination at the working point is independent of the gas density since the coverage of the chemically absorbed layer is close to unity***". If one neglect the recombination of the atoms on the sample tube and extension tube, thus one has:

$$I_{tot}^{BRP} = c_{BRP}\rho_a^{cell} \propto \frac{c_{BRP}}{\alpha_r} \cdot \Phi_a^{ABS} \tag{2.31}$$

in which c_{BRP} is the geometry acceptance and detection efficiency of the BRP detector, ρ_a^{cell} is the number density of the hydrogen/deuterium atoms in the cell, Φ_a^{ABS} is the ABS injected beam intensity. By comparing Eqn. 2.31 with Eqn. 2.14, one could find that both the TGA and the BRP are monitors of the atomic beam intensities which are injected by the ABS into the storage cell. In fact, from the study in [13], which is plotted in Fig. 2.11, most of the particles detected by the TGA have at least scattered on the extension tube because of the 7 titled angle of the TGA to the sample and extension tube axis, while most of the particles detected by the BRP are coming directly from the cell and sample tube. As the extension tube has a

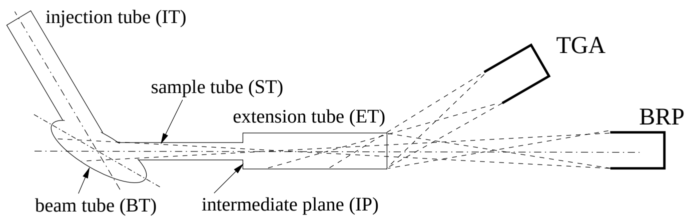

Figure 2.11: [13] Schematic View of the Geometrical Acceptance of BRP and TGA: Atoms or molecules entering the TGA had their last wall collision in the extension tube, while the acceptance of the BRP contains atoms from ansy position between the center of the beam tube until the end of the extension tube.

unwanted thermal contact with the dipole magnet which made it has a much higher temperature ($> 180K$) than the cell working temperature ($100K/80K$), the BRP is a better device to monitor the ABS beam intensity than the TGA.

2.5.3 BRP Calibration

The calibration requires the determination of the efficiencies of all transitions as well as a determination of the transmission probabilities of the sextupole system. For the SFT unit, two (five) efficiencies are required in case of hydrogen (deuterium), namely ϵ_{s14} and ϵ_{s24} (ϵ_{s16}, ϵ_{s26}, ϵ_{s35} and the two efficiencies of the SFT double transition ϵ_{s25r25} and ϵ_{s25r36}). The MFT unit can also be described by several separate transitions. The hydrogen MFT $1-3$ is described by the values of ϵ_{m13r12} and ϵ_{m13r23} and the same for the MFT $2-3$. The description for the MFT in case of deuterium requires three efficiencies[11].

The total number of efficiencies N_{eff} which need to be determined is 10 in case of hydrogen and 41 in case of deuterium[12]. The number of different transition states of the BRP and thus measurable count rates N_{BRP} is 11 for hydrogen and 29 for deuterium[13]. As the ABS can be operated with several spin state modes (N_{ABS}) and if all N_{BRP} BRP count rates for all possible BRP transition states are measured, then $N_{BRP}{\cdot}N_{ABS}$ equations are obtained. For calibration it is necessary to determine $N_{eff} + N_{hfs}{\cdot}N_{ABS}$ unknowns. The degree of freedom N_f is given by:

$$N_f = (N_{BRP} - N_{hfs}){\cdot}N_{ABS} - N_{eff} \tag{2.32}$$

for $N_f \geq 0$ the system of equations can be solved[13]. 7 (5 or 6) ABS operation modes are typically used for a hydrogen calibration measurement which result in $N_f = 39$ (74 or 97). Calibration measurements are performed periodically to check that the efficiencies are stable in time.

The beam blocker ensures that atoms with $m_J = -1/2$ are not able to reach the detector. For the transmission probabilities of different hyperfine states through the sextupoel magnet system, only the ratio σ_2/σ_1 is required for hydrogen and σ_2/σ_1 for deuterium[47]. For example, the transmission probabilities ratio σ_2/σ_1 for hydrogen was determined by minimizing the χ^2 value of the calibration results. The result[47] for working temperature of $95K$ was $\sigma_2/\sigma_1(95K) = 1.029 \pm 0.0015$. The result BRP transition units efficiencies measured during 1997 hydrogen running are listed in Tab. 2.3, while the sextupole transmission ratio is $\sigma_2/\sigma_1 = 1.029$.

[11] Due to the limited space, the static field coils of both BRP transition units are positioned close to each other and can not be controlled independently with the required precision. Namely the setting of the static field of the SFT unit changes the field of the MFT unit by some percent, so that the setting of the static field of the MFT must be chosen separately for each SFT magnetic field setting. Separate efficiencies of the MFT units need to be determined for each SFT setting as the transition efficiencies depend on the exact field. For example, the notations for MFT $1-3$ are $\epsilon_{m13r13c14}$ and $\epsilon_{m13r13c24}$ which describe the MFT $1-3$ where the SFT are set to the values of the SFT $1-4$ and SFT $2-4$ respectively.

[12] These large numbers are necessary because of the crosstalk between the magnetic fields of the transition units. If the crosstalk could be avoided, only 6 efficiencies are required for hydrogen and 14 for deuterium.

[13] If the crosstalk could be avoided, the number of different transition states of the BRP N_{BRP} is 9 for hydrogen and 20 for deuterium.

Name	MFT-B	SFT-B	Efficiency	Error
ε_{s14}	-	1-4	99.3	1.34
ε_{s24}	-	2-4	101.0	1.03
$\varepsilon_{s13r12c14}$	1-3	1-4	101.0	1.03
$\varepsilon_{s13r23c14}$			98.6	1.41
$\varepsilon_{s23r12c14}$	2-3	1-4	-1.0	1.13
$\varepsilon_{s23r23c14}$			94.9	1.23
$\varepsilon_{s13r12c24}$	1-3	2-4	99.9	0.42
$\varepsilon_{s13r23c24}$			90.3	0.82
$\varepsilon_{s23r12c24}$	2-3	2-4	0.0	1.10
$\varepsilon_{s23r23c24}$			97.4	1.04

Table 2.3:
BRP transition units efficiencies [%] measured during the 1997 hydrogen running fixing the sextupole transmission ratio to $\frac{\sigma_2}{\sigma_1} = 1.029$. Each efficiency is shown along with an explanation of the MFT and SFT static field setting.

2.6 The Luminosity Moniter

The HERMES luminosity monitor [50] is a part of the HERMES spectrometer and detects the Bahabha scattering ($e^+e^- \rightarrow e^+e^-$) and the positron electron annihilation ($e^+e^- \rightarrow \gamma\gamma$) of the HERA positron beam with the electrons of the target gas under small angles. If the HERA storage ring is filled with electrons, the detected process is represented by the Moeller scattering ($e^-e^- \rightarrow e^-e^-$). The number of events is proportional to the electron density inside the storage cell and therefore to the number of nucleons in the target.

The luminosity monitor together with the unpolarized gas feed system can be used to measure the absolute ABS beam intensity, which is briefly described in Sec. 2.3.

Chapter 3

TGA Calibrations in HERMES 2002 Running

3.1 TGA Emission Current Scan

By ionizing atoms and molecules into ions and measuring the count rates of different ions which have masses of 1, 2 or 18 amu., the TGA measures atomic and molecular signals. Therefore the TGA count rates depend on the ionization efficiency and thus on the emission current of the ionizing electric gun, the so-called *TGA emission current*. The dependence of the TGA count rates on the TGA emission current can be described by functions $F_{a,m}(I_{emis})$, in which the subscripts denote the atomic (a) and molecular (m) signals respectively,

$$S_{a,m} \propto F_{a,m}(I_{emis}) \tag{3.1}$$

The dependence on I_{emis} is not necessarily linear, as space charge effects in the electron gun can lead to a change in the trajectories of the ionizing electrons and thus to a change in the ionization efficiency. To describe the nonlinear behavior, the dependence of $s_{a,m} = S_{a,m}/I_{emis}$ on I_{emis} is usually used, which is represented by a function $f_{a,m}$. To determine $f_{a,m}$, the TGA emission current is varied and in the same time the TGA measures the atomic and molecular signals when keeping the ABS running at stable status[1], which is called TGA emission current scan. In reality, as the count rates of the real molecular signals S_m is 3 orders less than the count rates of the molecular background signals $S_m^{background}$, f_m is determined by the dependence of $s_m^{background}$ on I_{emis} achieving a much better statistical error[2].

The upper 3 plots of Fig. 3.1 show the procedure of the measurement, in which the horizontal ordinates represent the time in units of minutes, the vertical ordinates represent I_{emis}, $S_m^{background}$ and S_a respectively. The lower 2 plots of Fig. 3.1 are the

[1]One measurement usually takes less than two hours, and we could assume the output of the ABS is not changing.

[2]Here takes the assumption that the count rate of the TGA molecular signals has the same dependence on the TGA emission current as the one of the TGA molecular background. The validity of this assumption depends on the fact that the molecular background detected by the TGA are molecules recombined in the TGA detection chamber, which is the same as the molecular signals from the point of view of the TGA detecting device.

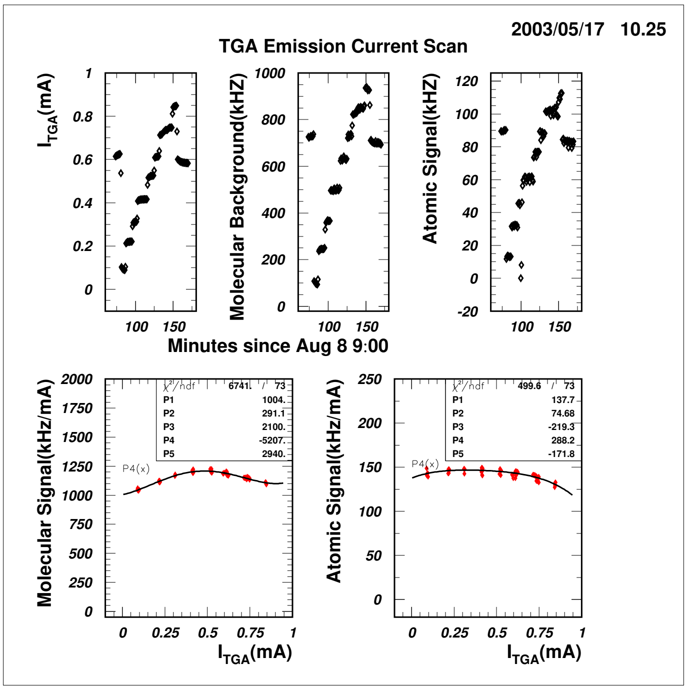

Figure 3.1: Dependence of TGA Count Rates on TGA Emission Current. TGA emission current is varied from $0.1mA$ to $0.9mA$, The upper 3 plots of Fig. 3.1 present the procedure of the measurement, in which the horizontal ordinates represent time in unit of minute, and the vertical ordinates represent I_{emis}, $S_m^{background}$ and S_a respectively. The lower 2 plots of Fig. 3.1 are the results of $S_m^{background}$ and S_a as functions of I_{emis}, and fits to the measured data with a polynomial of 4th degree.

results of $S_m^{background}$ and S_a as functions of I_{emis}, and fits to the measured data with a 4th degree polynomial. The results are:

$$\begin{aligned} f_a(I) &= f_a(0.6mA)\left[1.0212 + 0.1215I + 0.9613I^2 - 2.0759I^3 + 0.9720I^4\right] \\ f_m(I) &= f_a(0.6mA)\left[0.8842 + 0.3479I + 1.6653I^2 - 4.4141I^3 + 2.5168I^4\right] \end{aligned} \quad (3.2)$$

3.2 Background Pressure Calibration

As the HERMES gaseous target is located inside the HERA storage ring, the target storage cell is connected with the HERA beam pipe as one part of it (seen from Fig. 2.4. The pressure of the target storage cell gets a contribution from the gas background of the HERA beam pipe, which is not zero even when the gate valve between the ABS and the storage cell is closed. This pressure is called the *background pressure* which contributes to the total target storage cell pressure when the ABS works. When calculating the rest gas signals which is proportional to the target storage cell pressure, this background pressure has to be subtracted in advance.

In the former years, the background pressure of the target was determined by applying some requirements — such as the gate valve between the ABS and the target storage cell is closed, the gate valve between the BRP and the target storage cell is closed, the gate valve between the UGFS and the target storage cell is closed, etc — through all the data of the year and then taking the average value of the selected data, which did not satisfy the requirements for the background pressure measurements[3].

After August 2002, a new routine target calibration during the HERMES data taking begins per week, which is called background pressure calibration. The background pressure calibration is done by closing the gate valves of the ABS and the BRP to the storage cell for one hour, and the limit of the decreasing pressure is regarded as the background pressure. The target magnet and the spectrometer magnet have to be on during these calibrations because the readouts of the ion gauge depends on the external magnet field. The average value of the background pressure calibrations during HERMES 2002 running is used in the background pressure subtraction, which is[4]:

$$\begin{aligned} P_B^{PS3} &= 2.9 \pm 0.7 \times 10^{-9} mBar \\ P_B^{PS4} &= 3.6 \pm 0.6 \times 10^{-9} mBar \end{aligned} \tag{3.3}$$

3.3 Rest Gas Calibration

One contribution of the TGA molecular signals originates from the rest gas molecules which are diffusing within the target chamber due to the finite pumping speed. This part of molecules either comes from the recombined molecules or from molecules injected by the ABS directly. The rest gas distributes in the target chamber as well as the storage cell uniformly and is unpolarized. The contribution of the rest gas to the TGA molecular count rates ϕ_{rg} is proportional to the pressure of the target chamber:

$$\phi_{rg} = C_{rg} \cdot [p_{tc} - p_B] \tag{3.4}$$

in which the p_B is the background pressure of the target chamber, p_{tc} is the pressure of the target chamber, C_{rg} is a constant which gives the relationship between phi_{rg} and p_{tc}. As PS3 and PS4[5] have different pressure readout, thus C_{rg} should be analyzed separately for PS3 and PS4. To know the target polarization, it is necessary to know C_{rg}. By regulating the gas flow from the UGFS into the target cell and keeping the pressure in the target region as half, one and double respectively as the normal working pressure, C_{rg} are determined.

[3] After the gate valves to the target storage cell are closed, the pressure of the target storage cell decreases exponentially and slowly (one hour typically) to a stable limit. The decreasing pressure measured during this procedure satisfies these requirements applied, while only the stable pressure limit is the background pressure.

[4] The PS3 and PS4 refer to two pump stations which pump directly on the target region. One ion gauge in each pump station is used to measure the pressure, thus two C_{rg} are to be measured separately.

[5] The PS3 and PS4 refer to two pump stations which pump directly on the target region. One ion gauge in each pump station is used to measure the pressure, thus two C_{rg} are to be measured separately.

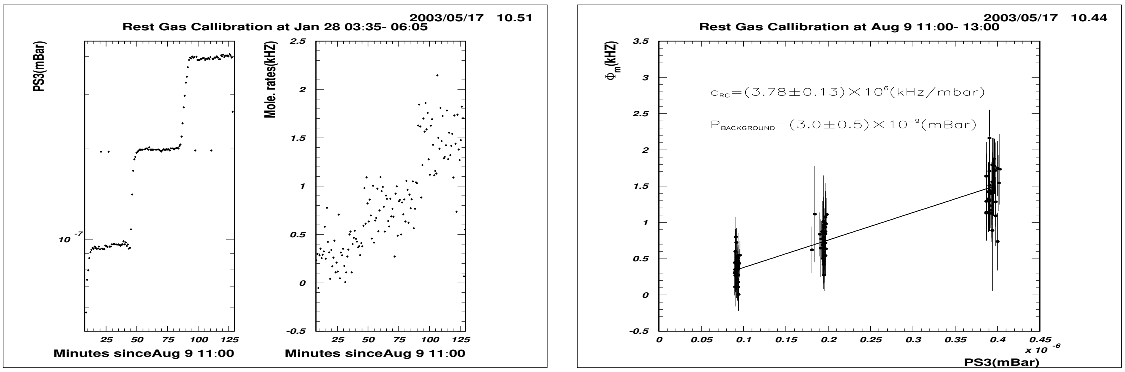

Figure 3.2: Rest Gas Calibration. By regulating the gas flow from the UGFS into the target cell and keeping the pressure of the target chamber as half, one and double respectively of the pressure of target normal working status. The left plot only shows the PS3 pressure changing with time, the middle plot shows the TGA molecular count rates changing with time, and the right plot shows the result fitted with Eqn. eqn:rest as $C_{rg}^{PS3}(I_{emis} = 0.6mA) = (3.78 \pm 0.13) \times 10^6 kHz/mBar$

The left and the middle plots of Fig. 3.2 show the procedure of the rest gas calibration. The left plot only shows the PS3 pressure p_{tc}^{PS3} changing with the time, the middle plot shows the TGA molecular count rates changing with the time. In the analysis, the background pressure p_B^{PS3} has to be subtracted first and the TGA molecular count rates also are normalized for the TGA emission current. The right plot of Fig. 3.2 shows one of the fitted results:

$$C_{RG}^{PS3}(I_{emis} = 0.6mA) = (3.78 \pm 0.13) \times 10^6 kHz/mBar \tag{3.5}$$

The results of the rest gas calibrations in HERMES 2002 running are listed in Tab. 3.1. As the TGA channeltron high voltage was changed from 1900V to 2100V at 2002.12.13, which for sure changed the multiplication of the channeltron and the C_{rg} systematically. The cell temperature was changed from 100k to 82k at 2003.1.10, which changed the value of the cell temperature of $g(T_{cell}, T_{ET})$ (Eqn. 2.13). After taking account the different TGA channeltron high voltages, the C_{rg}^{PS3} and C_{rg}^{PS4} measured under the same TGA channeltron voltage were still not stable for these calibrations as listed in Tab. 3.1, which were due to the fact that the ion gauges were not working stable and were free flowing within a long period.

For the whole HERMES 2002 running, an average value of C_{RG}^{PS3} and one of C_{RG}^{PS4} were first normalized on the temperature function Eqn. 2.13 $g(T, T_{ET})$, in which the normalized temperatures are taken as,

$$T_{norm} = 100K, T_{ET,norm} = 180K$$

then averaged via Eqn. 3.6. The results were used in the following Ballistic Flux Calibrations as well as the data production.

$$\begin{aligned} \overline{x} &= \frac{\sum_i w_i \cdot x_i}{\sum_i w_i}, \quad \delta\overline{x} = \left(\sum_i w_i\right)^{-1/2} \\ w_i &= 1/(\delta x_i)^2 \end{aligned} \tag{3.6}$$

Rest Gas Calibration				
No.	date	$C_{rg}^{PS3}(10^6 kHz/mBar)$	$C_{rg}^{PS4}(10^6 kHz/mBar)$	$T_{ET}(K)$
1	2002.08.07.	4.17 ± 0.18	4.93 ± 0.21	194.9
2	2002.08.09.	3.78 ± 0.13	4.53 ± 0.15	194.8
3	2002.09.15.	3.15 ± 0.12	4.15 ± 0.10	197.5
4	2002.10.25.	4.43 ± 0.15	3.97 ± 0.14	189.3
5	2002.11.06.	3.09 ± 0.11	3.98 ± 0.14	186.5
6	2002.11.18.	2.74 ± 0.12	3.90 ± 0.17	193.5
7	2002.11.21.	3.01 ± 0.14	3.24 ± 0.15	197.0
8	2002.11.27.	3.44 ± 0.12	3.50 ± 0.12	198.0
9	2002.12.11.	3.54 ± 0.15	4.48 ± 0.18	196.7
The TGA channeltron HV is changed from 1900V to 2100V since 2002.12.13				
9	2002.12.15.	3.65 ± 0.17	4.84 ± 0.23	207.0
10	2003.01.03.	3.74 ± 0.18	4.85 ± 0.23	191.0
The cell temperature is changed from 100k to 82k since 2003.1.10				
11[a]	2002.01.18.	3.54 ± 0.21	4.77 ± 0.29	185-195
12	2002.01.28.	3.61 ± 0.17	5.04 ± 0.24	180.5

Table 3.1: Summary of the Rest Gas Calibrations in HERMES 2002 Running. The results have been normalized to the TGA emission current of $0.6mA$. (a) In this calibration the Extension Tube temperature changed in from 185K to 195K.

In HERMES 2002 running the results of averaging are:

TGA high voltage (V)	$\overline{C_{rg}^{PS3}} \times 10^6 (kHz/mBar)$	$\overline{C_{rg}^{PS4}} \times 10^6 (kHz/mBar)$
1900	3.49 ± 0.54	4.10 ± 0.51
2100	3.73 ± 0.58	4.97 ± 0.62

3.4 Ballistic Flux Calibration

Another contribution to the TGA molecular count rates comes from molecules directly injected by the ABS into the target cell, which is denoted by ϕ_{ball} (see Subsec. 2.4.2 and Eqn. (2.17-20)). By changing the working status of SFT 2-4 and MFT 1-3 between the two ABS sextupole magnet subsystems in 3 steps,

- neither SFT nor MFT works, $|1\rangle + |2\rangle$ is injected into the storage cell;
- SFT works and MFT does not work, $|1\rangle$ is injected into the storage cell;
- both SFT and MFT work, 'zero'[6] is injected into the storage cell.

[6] Which means non hydrogen atoms are to be injected by an ideal ABS.

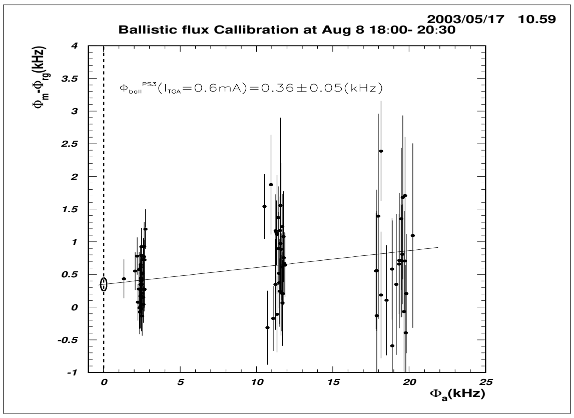

Figure 3.3: Ballistic Flux calibration. The TGA atomic count rates and molecular count rates have been normalized for the TGA emission current. The ellipse is $\phi_{ball}(I_{emis} = 0.6mA) = 0.36 \pm 0.05kHz$.

As in the calibration only the working status of the ABS HFTs are changing, ϕ_{ball} remains as a constant. Meanwhile the conclusion of the recombination studies done on the HERMES target[32] are that "***recombination at the working point is independent of the gas density since the coverage of the chemical absorbed layer is close to unity***", α_r is a constant independent of the gas density. Thus there is:

$$\phi_m^{(i)} - \phi_{rg}^{(i)} - \phi_{ball} \propto \phi_a^{(i)} \tag{3.7}$$

Ballistic Flux Calibration				
No.	date	$\phi_{ball}^{PS3}(kHz)$	$\phi_{ball}^{PS4}(kHz)$	$T_{ET}(K)$
1	2002.08.08.	0.348 ± 0.062	0.355 ± 0.062	194.7
2	2002.10.12.	0.346 ± 0.062	0.346 ± 0.062	187
3	2002.10.25.	0.35 ± 0.08	0.35 ± 0.08	191
4[a]	2002.11.06.	0.19 ± 0.07	0.21 ± 0.07	
5	2002.11.17.	0.41 ± 0.103	0.362 ± 0.083	195
6	2002.11.18.	0.355 ± 0.051	0.364 ± 0.051	194.6
The TGA channeltron HV is changed from 1900V to 2100V since 2002.12.13				
7[b]	2002.11.27.	0.318 ± 0.049	0.348 ± 0.049	
8[c]	2002.12.14.	0.36 ± 0.11	0.36 ± 0.11	
9	2003.01.03.	0.29 ± 0.107	0.271 ± 0.107	189.7
The cell temperature is changed from 100k to 82k since 2003.1.10				
10	2003.01.11.	0.313 ± 0.137	0.321 ± 0.137	181
11	2002.01.18.	0.49 ± 0.139	0.422 ± 0.139	184
12	2002.01.28.	0.426 ± 0.087	0.445 ± 0.087	179.4

Table 3.2: Summary of Ballistic Flux Calibrations in HERMES 2002 Running. The results have been normalized for the TGA emission current to $0.6mA$. (a) 10 minutes after an access; (b) begin at 01:00, nozzle regeneration 5 hours ago; (c) A nozzle regeneration 10 minutes ago.

The analysis for one Ballistic Flux calibration is shown in Fig. 3.3. First $\phi_m^{(i)} - \phi_{rg}^{(i)}$ and $\phi_a^{(i)}$ [7] normalized for the TGA emission current for the 3 steps are calculated, then they are fit as a straight line, the cross-point of the fitted line with the y axis is $\phi_{ball}(I_{emis} = 0.6mA)$. The result is:

$$\phi_{ball}(I_{emis} = 0.6mA) = 0.36 \pm 0.05kHz \tag{3.8}$$

The results of the ballistic flux calibrations in HERMES 2002 running are listed in Tab. 3.2. ϕ_{ball}^{PS3} and ϕ_{ball}^{PS4} result from C_{rg}^{PS3} and C_{rg}^{PS4} respectively. Moreover, the TGA channeltron high voltage was changed from 1900V to 2100V since 2002.12.13; which changed the multiplication of the channeltron and changed the C_{rg} systematically. The cell temperature was changed from 100k to 82k since 2003.1.10, which changed the cell temperature value in function $g(T_{cell}, T_{ET})$ (Eqn. 2.13).

Applying the same temperature normalization and averaging equations (Eqn. 3.6) as of Rest Gas Calibrations, the average Ballistic Flux Calibrations are:

TGA high voltage (V)	$\overline{\phi_{ball}}(kHz)$
1900	0.36 ± 0.03
2100	0.37 ± 0.06

3.5 Temperature Scan and κ

In Sec. 2.4 it was mentioned that the TGA has different sensitivities to atoms and molecules. To get the correct atomic fraction relative to the molecular fraction of the target, it is important to know the ratio of the TGA sensitivity for the atoms to the one for the molecules, defined as κ.

As the ABS intensity is constant during normal operation, by varying the cell temperature thus varying α_{TGA}, κ can be determined by a linear fit of S_m versus

[7] Here the superscripts (i) refers to the step number.

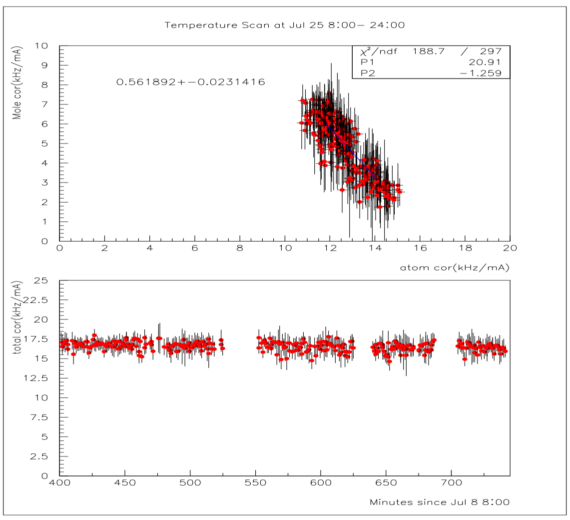

Figure 3.4: κ measurement. By varying the cell temperature α_{TGA} is changed. In the upper plot the TGA atomic count rates and molecular count rates normalized for the TGA emission current are plotted as horizontal coordinates and vertical coordinates. The slope of the fitted straight line equals $\sqrt{2}\kappa$ and the result is $kappa = 0.56 \pm 0.02$. The lower plot is the sum $S_a + \sqrt{2}\kappa S_m$ which applied the fitted κ.

S_a which both have been normalized to the TGA emission current and temperature function $g(T)$ (Eqn. 2.13):

$$S_a + \sqrt{2}\kappa S_m = const \propto \phi_{ABS} \tag{3.9}$$

in which $S_a + \sqrt{2}\kappa S_m$ is proportional to the ABS intensity ϕ_{ABS}. The slope of the fitted straight line equals $\sqrt{2}\kappa$, as plotted in Fig. 3.4:

$$\kappa = 0.56 \pm 0.02 \tag{3.10}$$

Chapter 4

Influence of a New Correction Coil to the HERMES Acceptance — Inclusive DIS

4.1 Introduction

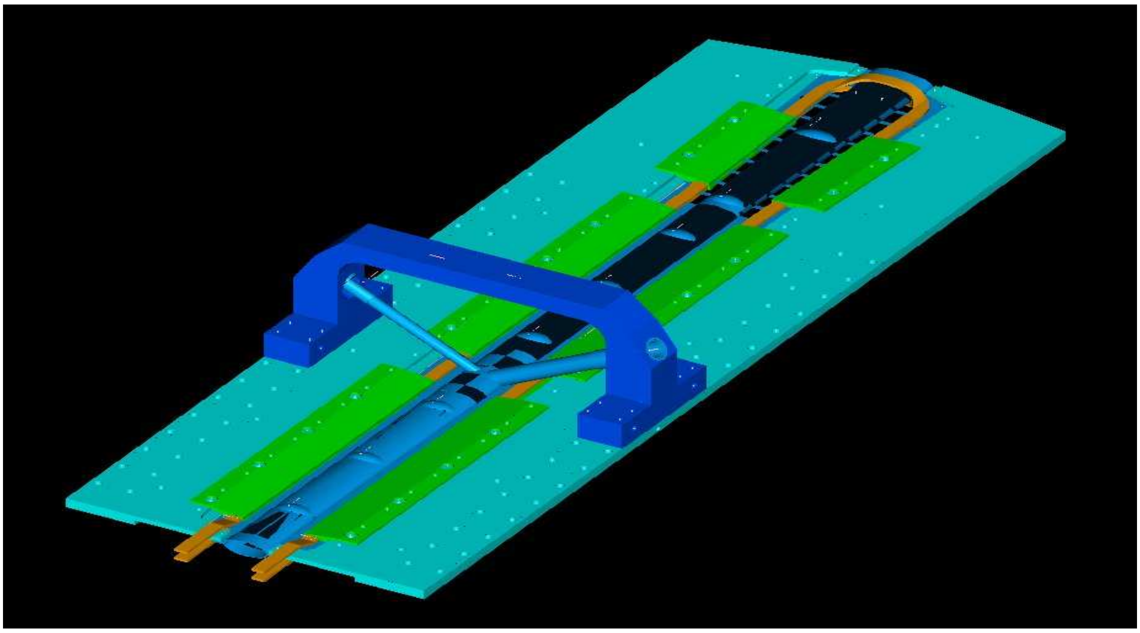

Figure 4.1: 3D view of the storage cell with the correction coil and the support frame which have been installed in the HERMES experiment during the HERA long shutdown of 2003 March to 2003 July.

In the case of a transverse magnetic field, the bunch structure of the positron beam will induce additional σ resonance in the polarized target[56]. The observation of 1% beam-induced nuclear spin depolarization in HERMES 2002 running[52] proved the existence of such kind of resonance. It has been proposed by the *Ferrara* group to compensate this kind of beam-induce depolarization by a correction coil.

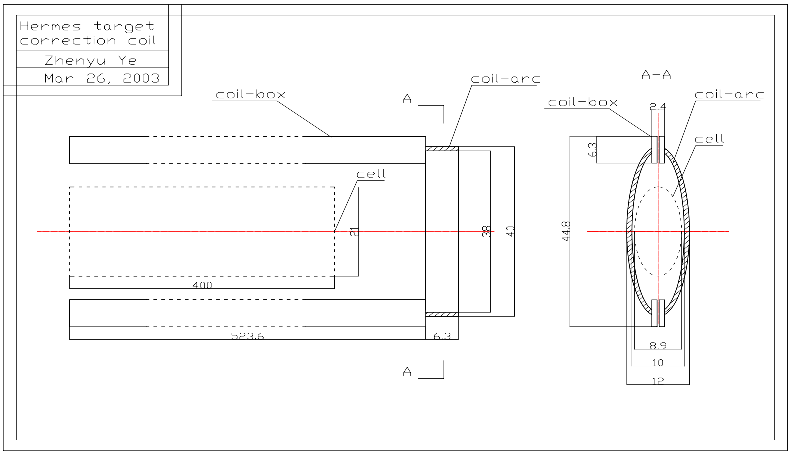

Figure 4.2: CAD drawing of the correction coil. The correction coil is made by copper, which has a density of $8.96g/cm^3$, a radiation length of $1.43cm$. The geometry parameters are listed in Tab. 4.1, which are taken from the hmc geometry file used in the MC simulation. The correction coil in the geometry file consists of 4 strips(coil_box) and an ellipse tube(coil_arc).

The 3D view of the new cell with the correction coil is plotted in Fig. 4.1.

The correction coil is made by copper, which has a density of $8.96g/cm^3$, a radiation length of $1.43cm$. The geometry parameters are listed in Tab. 4.1 and Fig. 4.2, which are taken from the hmc geometry file used in the MC simulation. The correction coil in the geometry file consists of 4 strips(coil_box) and an ellipse tube(coil_arc).

To study a possible influence of the correction coil to the acceptance of the HERMES spectrometer, two sets of MC data were generated[1], one with coil and the other without coil. One million of inclusive DIS events for each case are generated via gmcdis_NG with full tracking and simulating the transverse magnet to check

[1]by E. C. Aschenauer

Name	Number	Shape	Geometry(cm)	Center Position(cm)(x,y,z)
coil-arc	1	ELTU	out diameter(4.0,1.2) inner diameter(3.8,1.0) length 0.63	(0,0,52.7)
coil-box	4	Box	length along x 0.63 length along y 0.10 length along z 52.36	($\pm$1.93,$\pm$0.07,6.18)

Table 4.1: Geometry parameters of the Correction Coil. The parameters are taken from the hmc geometry file with which the MC data are generated. The correction coil is put in this geometry file with an approximation, i.e. the coil consists of 4 strips(coil_box) and an ellipse tube(coil_arc).

that there is not a bad surprise by adding a scattering center.

The particles, which go across the correction coil, will be multi-scattered thus affecting the reconstructed θ, ϕ and the vertex positions of the interactions. They will also deposit some of their energies in the coil thus affecting the reconstructed kinematics. The positron will have a chance to produce a shower when it goes across the coil. Events with multi-track showers may not be reconstructed[2].

There are three questions which have to be clarified:

- *Is the correction coil in the HERMES spectrometer acceptance?*
- *If the coil is in the HERMES acceptance, how many more events will get lost?*
- *How does the coil affect the reconstructed kinematics distribution?*

4.2 Definition of Kinematics

The HERMES experiment studies the spin structure of the nucleons by the *deep inelastic scattering* process:

$$e^+ + N \rightarrow e^{+'} + X \tag{4.1}$$

where a positron e^+ of energy $E \simeq 27.5GeV$ is scattered off a nucleon (proton, neutron), therefore exciting it to a hadronic final state X with an invariant mass W much larger than the nucleon mass M. If only the scattered positrons are detected, they are called *inclusive* DIS events.

The electromagnetic interaction in the approximation of one-photon exchange dominates at the HERMES energies. Using $\mathsf{k} = (E, \vec{k})$ ($\mathsf{k}' = (E', \vec{k}')$) to represent the four-momenta of the positron before (after) the scattering and $\mathsf{q} = (\mu, \vec{q})$ to represent the four-momentum of the exchanged virtual photon during the reaction, the DIS process can be characterized by the following Lorentz-invariant quantities:

$$q^2 = -Q^2 = (\mathsf{k} - \mathsf{k}')^2 \tag{4.2}$$

$$W^2 = (\mathsf{p} + \mathsf{q})^2 \tag{4.3}$$

As the HERMES experiment is an fixed-target experiment, $\mathsf{p} = (M, 0)$, and also because the positron energies E and E' are much larger than the positron mass m_e, thus we obtain in the nucleon rest system:

$$Q^2 \simeq 4EE' \sin^2 \frac{\theta}{2} = 2EE'(1 - \cos\theta) \tag{4.4}$$

$$W^2 = M^2 + 2M\mu - Q^2 \tag{4.5}$$

in which θ is the scattering angle of the positron, $\mu = E - E'$ is the energy of the virtual photon. Two dimensionless variables can be defined as:

$$y = \frac{\mathsf{p} \cdot \mathsf{q}}{\mathsf{p} \cdot \mathsf{k}} = \frac{\mu}{E} \tag{4.6}$$

$$x = \frac{Q^2}{2\mathsf{p} \cdot \mathsf{q}} = \frac{Q^2}{2M\mu} \tag{4.7}$$

[2]The HERMES reconstruction software is not designed to reconstruct an event if it has more than 20 tracks

Here y ($0 \leq y \leq 1$) is the fractional energy transfer from the positron to the nucleon and x ($0 \leq y \leq 1$) is the Bjorken scaling variable. The variable x can be interpreted as the fraction of the nucleon's light-cone momentum carried by the struck quark.

4.3 Monte Carlo procedure

The MC procedure is,

$$gmcdis\_NG \Longrightarrow hmc \Longrightarrow hrc \Longrightarrow wriDST$$

in which gmcdis_NG is a generator which uses Lepto6.5.1[53] to simulate the hard QCD processes (DIS, QCDC and PGF) and the new JetSet[54] version from PYTHIA6.2 to describe the fragmentation of quarks to hadrons. To account for radiative effects RADGEN[55] was included in the Monte Carlo generation.

hmc is the HERMES-developed MC package, which depends on Geant 3[57], to simulate the particle-matter interactions within the HERMES detectors, and the response of the detectors are digitalized and stored as the format as in the real experiment.

hrc is the standard reconstruction program developed by the HERMES which is used to reconstructed the information (momentum, particle identification, etc.) of the particles from the data of the experiment(also MC data).

In the end, the information of the reconstructed particles are written down by wriDST in the standard HERMES data format waiting for analyzing.

In this study[3], the target density distribution is taken into account and only scatted positrons are tracked, the radiation correction is still applied, but no fragmentation process happens. So they are inclusive MC data in which only the scattered positrons and the radiation γs are tracked by the detectors.

4.4 Results

Is the correction coil in the HERMES spectrometer acceptance?

The answer is *YES*, which can be seen from Fig. 4.3. This plot shows the x and y coordinates distribution at the $z = 323.6mm$ plane of the coil_arc front surface for the particles which are successfully reconstructed. The two boxes are the coil_box, the outer ellipses are the coil_arc and the inner represents the storage cell. The x-y positions are calculated from the generated vertex position and generated scattering angle θ and ϕ.

[3] The g1.ddl and g1MC.ddl are taken from worf.desy.de:/group01/mcgrp/writeMCDST_3.11/writeDST/ddl/ instead of the official HERMES version as these MC data are generated with *g1MCluster* entity which is only available with the g1MC.ddl file used here.

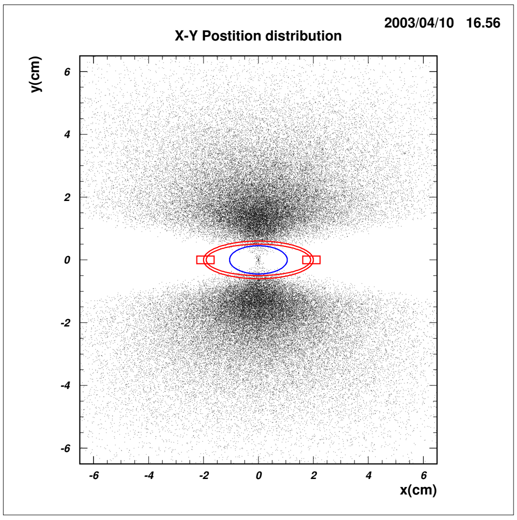

Figure 4.3: x-y position distribution of the positron at the start-plane of the coil_arc. The x and y are calculated from the generated data.

If the coil is in the HERMES acceptance, how many more events will get lost?

For this question, the answer is *"the effect to the whole data is negligible"*, which can be proved by Tab. 4.2. Tab. 4.2 lists the ratio of different kind of events. We can see that although the reconstruction or detection efficiency is 22.9% without coil and 19.1% with coil of the events that the scattered positrons go across the coil, only around 0.12% more events of all events are lost because only 1.2% positrons go across the coil.

Also because of the efficiency of reconstruction of the cross-coil events, 23% (even there is no coil there), is much lower than the average efficiency, 71.8%. So for the successfully reconstructed events (which is corresponding to the real data) the part which cross the coil is less than 0.4%. The influence of the coil only affect this 0.38% events for our data.

Ratio	With Coil	Without Coil
ALL_{rec}/ALL_{gen}	0.7170	0.7182
$Coil_{rec}/Coil_{gen}$	0.1913	0.2292
$Coil_{gen}/ALL_{gen}$	0.0116	0.0118
$Coil_{rec}/ALL_{rec}$	0.0031	0.0038

Table 4.2: Weight ratio for different kinds of events, *All* refers to all the events and *Coil* refer to the events in which the positrons go across the coil. *gen* refers to all the generated events, and *rec* refers to the events that have been successfully reconstructed. Kinematic cuts of $W^2 > 4GeV$ and $y < 0.93$ are applied.

How does the coil affect the reconstructed kinematics distribution?

Fig. 4.4 plots the generated and reconstructed kinematics without and with the coil respectively. The two lines in the plots represent the generated kinematics by gmcdis_NG, in which the one with shadowed area represents the part that scattered positrons go across the coil, and the other represents all the events. The triangles are the reconstructed kinematics of all the reconstructed events, The solid cycles are the reconstructed kinematics of all the reconstructed events in which the scattered positron go across the coil. The distributions of the reconstructed distribution have been normalized to the generated distributions according to the weights listed in Tab. 4.2. Kinematic cuts of reconstructed $W^2 > 4GeV^2$ and $y < 0.93$ are applied together with the requirement that one and only one track are reconstructed, as less than 0.1% events have more than one tracks reconstructed.

In Fig. 4.5 the reconstructed kinematics distributions with the coil and without coil are plotted. Up, cross-coil reconstructed kinematics distribution without the coil (line) and with the coil (solid cycle). Bottom, all reconstructed kinematics distribution without the coil (line) and with the coil (solid cycle). The distributions with the coil are normalized to the ones without the coil according to the generation weights of each case. After normalizing the data with coil to the data without coil, the difference of all reconstructed kinematics distributions between with coil and without coil are plotted in Fig. 4.6, in which $\Delta N_i/N_i = \left(N_i^{coil} - N_i^{nocoil}\right)/N_i^{nocoil}$ and i is the bin number.

By comparing the distributions without and with the coil, we can see (up plot of Fig. 4.5)that although the coil does affect the kinematics distribution of the positrons which go across the coil, especially the large value region of the p plot and the small value region of W^2 and y. But concerning that events in which positrons go across the coil is only 1.2% of all the events, and the reconstruction efficiency of the cross-coil events (even though there is not the coil), 22.9% is much less than the average reconstruction efficiency of 71.8%, the influence to the total kinematics distribution is very small (less than 0.3% in most of the kinematic regions), which are plotted in Fig. 4.7 which is gotten by multiplying the up plot of Fig. 4.6 for the cross-coil events by a factor of 0.31%.

Conclusion

From this study we can conclude that the correction coil has only little influence to the HERMES acceptance of the scattered positrons, namely around 0.1% events are lost and the bias to the reconstructed kinematic distributions is less than 0.3%. On the other side, the correction coil does have an influence to the Lambda Wheel detector, because Λs have a finite life time (corresponding to an average life range of $7.8cm$. Hence about 20% Λs are estimated to get lost by installing the coil[58]. The HERMES council decided to install the cell with the correction coil arguing that it is important to not have 1% beam-induced target depolarization and also thus to achieve a 2% smaller target polarization systematic error.

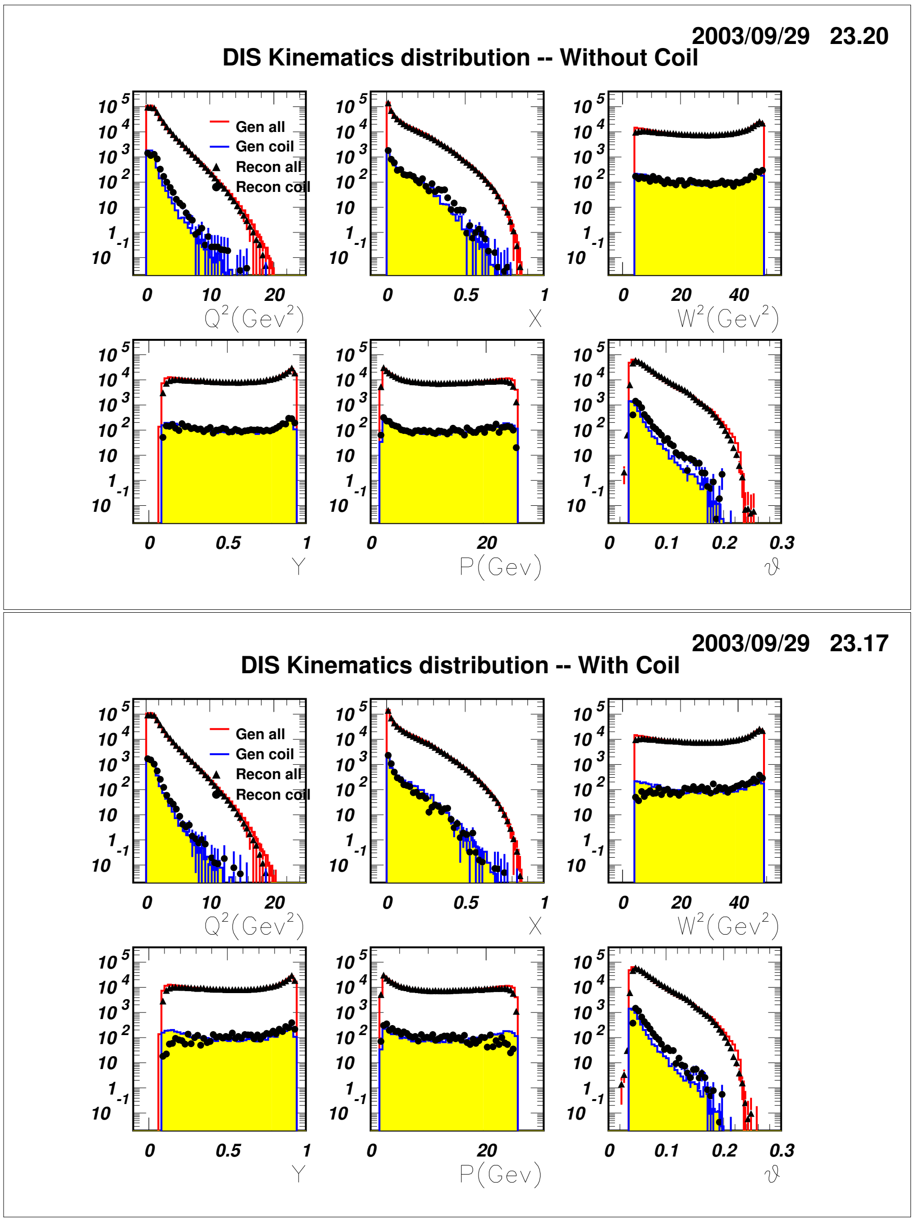

Figure 4.4: Generated and reconstructed kinematics distributions without (up) the coil and with (bottom) the coil. The distributions of the reconstructed data have been normalized to their generated data according to the weights listed in Tab. 4.2.

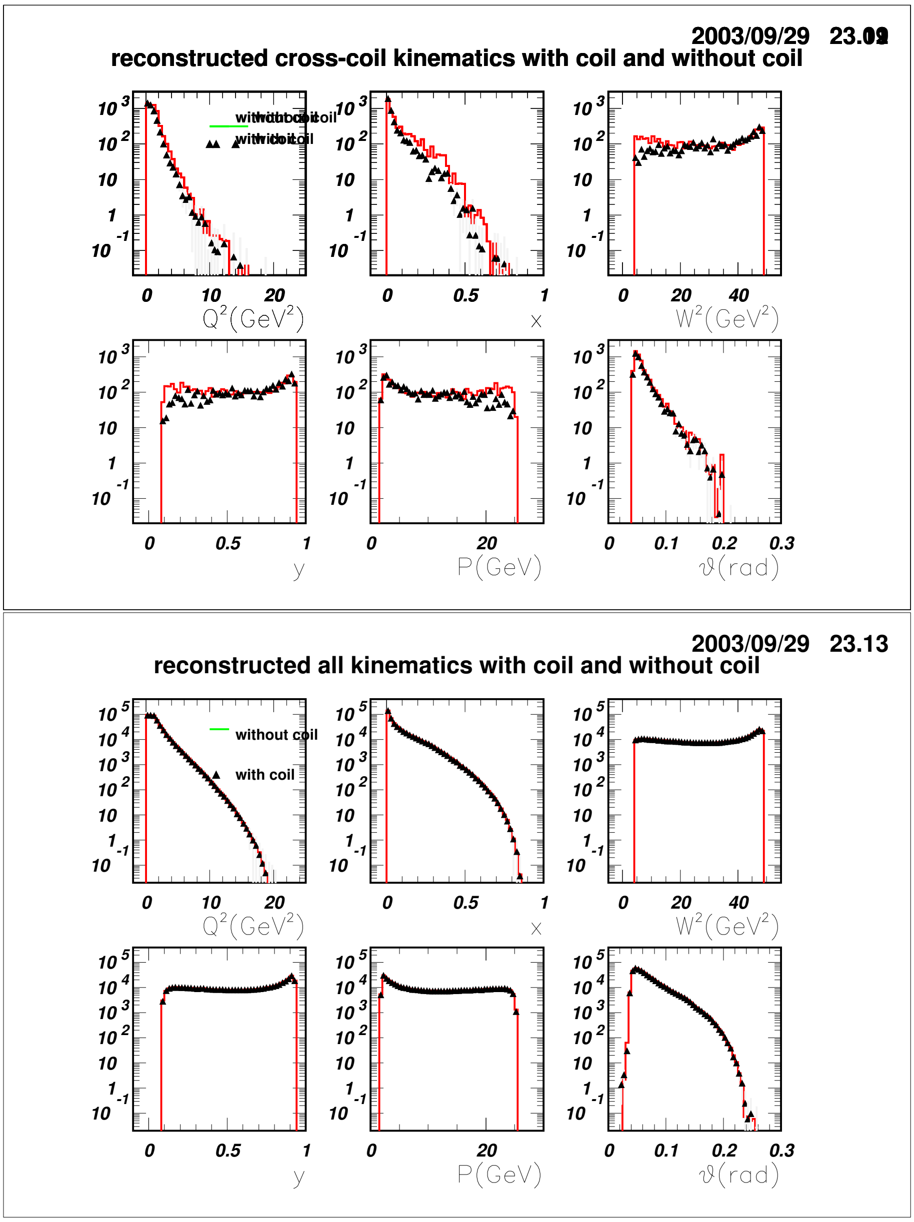

Figure 4.5: Reconstructed kinematics distributions between without and with the coil. Up, cross-coil reconstructed kinematics distribution without coil (line) and with (solid cycle) the coil. Bottom, all reconstructed kinematics distribution without (line) and with the (solid cycle) coil (Also look at Fig. 4.6.). The distributions with the coil are normalized to the ones without the coil according to their weights of generation.

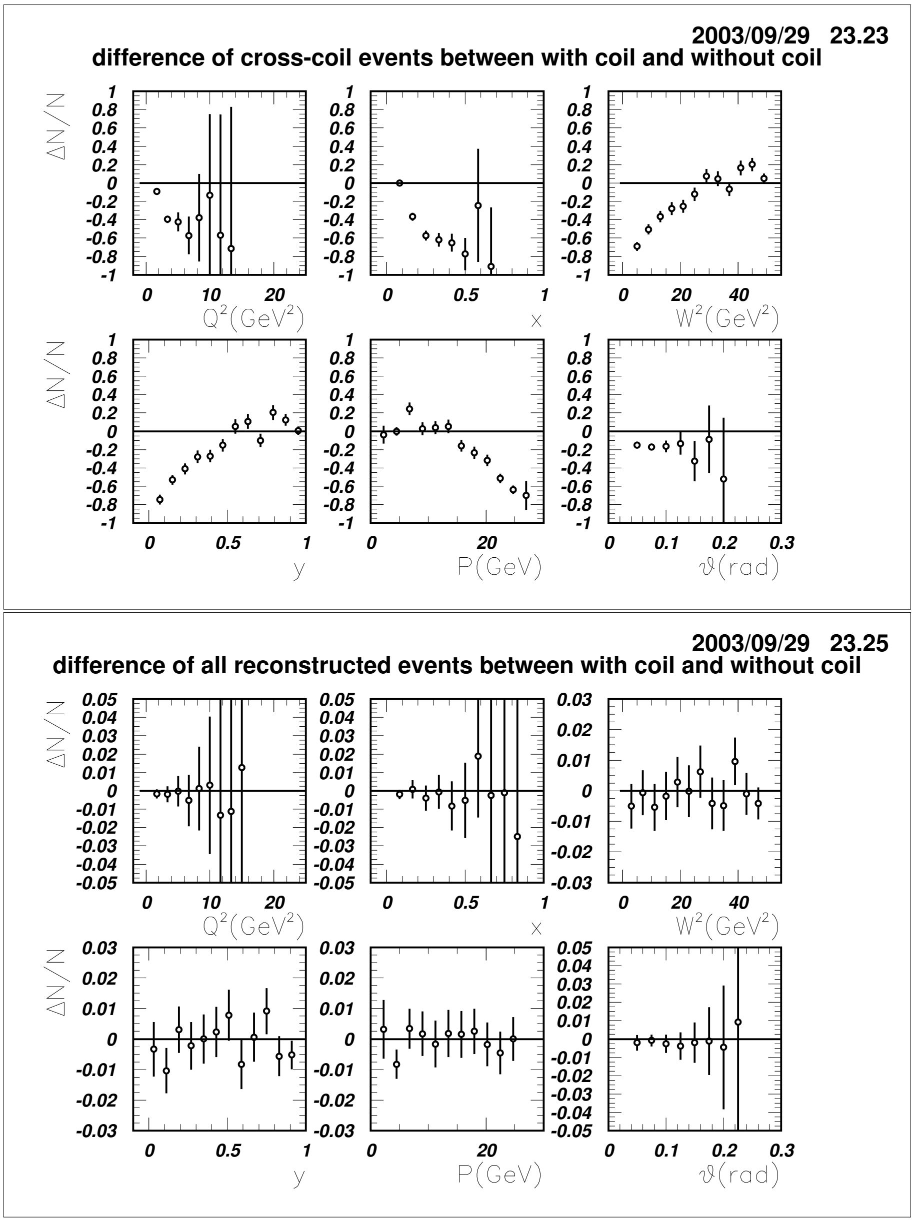

Figure 4.6: Difference of all reconstructed kinematics distributions between with coil and without coil. Also look at the plots of Fig. 4.5.

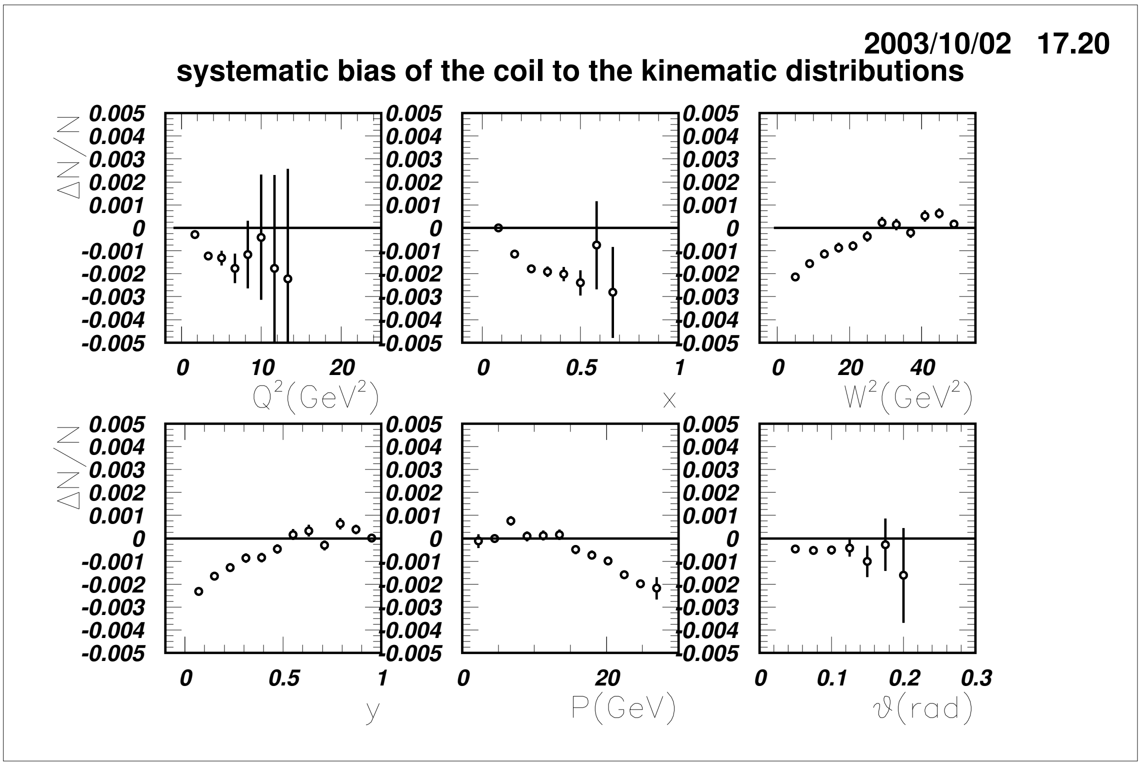

Figure 4.7: System Bias of the Coil to the Reconstructed Kinematic Distributions.

Chapter 5

Conclusion

This document presents the author's work on the HERMES hydrogen target. The calibration procedures of the HERMES target gas analyzer (TGA) are introduced, including TGA emission current scan, background pressure calibration, rest gas calibration, ballistic flux calibration and temperature scan. The results of the HERMES 2002 running are summarized, which are are used in the HERMES data production.

During the HERMES 2002 running, a 1% beam-induced target depolarization was observed. To compensate this effect, a correction coil which surrounds the target cell was designed by the Ferrara group. To study the influence of the correction coil to the acceptance of the HERMES spectrometer, two sets of 1000,000 inclusive DIS (deep inelastic scattering) Monte Carlo events were produced, one with coil and the other without coil to make sure that there is not a bad surprise by adding a scattering center in the HERMES experiment. By comparing the respective distributions of the reconstructed kinematics, we find that the correction coil has only little influence to the HERMES acceptance of the scattered positrons, namely around 0.1% events are lost and the bias to the reconstructed kinematic distributions is less than 0.3%. Consequently the HERMES council decided to install the correction coil in the 2003 HERA shutdown.

Appendix A

Geometry of Target Harware

The cross section S of an elliptical shaped tube of radius $a \times b$ is given by:

$$S = \pi \, a \, b \,,$$

and its circumference U approximately by:

$$U \simeq \pi \, [1.5 \, (a + b) - \sqrt{ab}] \,.$$

The conductance is given by[13]:

$$C = \frac{16}{3\sqrt{2\pi}} \, \frac{S^2}{UL + \frac{16}{3}S} \sqrt{\frac{kT}{m}} \,. \tag{A.1}$$

	beam tube	sample tube	injection tube	extension tube
radius R/mm	10.5×4.45	2.5	5.0	5.0
length L/mm	200	100	100	124
cross section mm^2	223.2	19.63	78.54	78.54
circumference mm	64.94	44.25	18.85	31.4
conductance C	0.682	0.291	0.0446	0.278
$\delta l = 4\,\frac{S}{U}(mm)$	13.75	5	10	10
$\epsilon = \frac{\sqrt{3}}{4}\,\frac{S}{U}$	25.2	34.6	17.3	20.8

Table A.1: Geometry of the HERMES storage cell. The conductances have to be multiplied by a factor $\sqrt{T_{[K]}/m_{[amu]}}$ to obtain meaningful values; the unit is l/s.

	z-pos	length	inn. radius	segments
Nozzle	5		1	
Collimator	50		3.7	
1. Magnet	63	30	4.3/5.2	12
2. Magnet	113	55	6.0/8.0	12
3. Magnet	188	75	8.35/12.5	12
4. Magnet	613	75	13.3	24
5. Magnet	728	85	13.3/11.0	24
Inj. tube	1183	50	5.0	

Table A.2: Geometry of the Atomic Beam Source[61]. All dimensions are given in $[mm]$. All magnets have a fill factor f of $f = 0.98$ and a magnetization of $1.132\,T$.

Stage	Pumps	$S_{nom}(l/s)$	$p_{op}(mbar)$
I	2×turbo	2×2200	1.2×10^{-4}
II	2×turbo	2×1000	2.0×10^{-5}
III	1×turbo	2200	1.8×10^{-6}
	+1×cryo	3500	
IV	1×turbo	360	1.5×10^{-7}
	+2×cryo	2×1500	

Table A.3: The HERMES ABS differential vacuum system. S_{nor}-nominal pumping speed, p_{op}-pressure at normal operation (dissociator throughput $1.5 mbar{\cdot}l/s$).

	z-pos	length	radius	B_{pt}
Sample tube	0	100	2.5	
Ext. tube	100	120	5.0	
Beam blocker	850	1	4.5	
1. Magnet	851	70	12.5	$1.45\,T$
2. Magnet	1056	110	12.5	$1.45\,T$
Detector	1455	-	4×8	

Table A.4: Geometry of the Breit-Rabi Polarimeter. All dimensions are given in $[mm]$.

Appendix B

Physical Constants

Quantity	Symbol, equation	Value
speed of light in vacuum	c	$299\,792\,458\, m\, s^{-1}$
plank constant	h	$6.626\,075\,5(40) \times 10^{-34}\, J\, s$
plank constant, reduced	$\hbar$	$1.054\,572\,66(63) \times 10^{-34}\, J\, s$
electron charge magnitude	e	$1.602\,177\,33(49) \times 10^{-19}\, C$
electron mass	m_e	$9.109\,389\,7(54) \times 10^{-31}\, Kg$ $= 0.510\,999\,06(15)\, MeV/c^2$
proton mass	m_p	$1.672\,623\,1(10) \times 10^{-27}\, Kg$ $= 938.272\,31(28)\, MeV/c^2$ $= 1.007\,276\,470(12)\, u$ $= 1836.152\,701(37)\, m_e$
deuteron mass	m_d	$1875.613\,39(57)\, MeV/c^2$
atomic mass unit	u	$1.660\,540\,2(10) \times 10^{-27}\, Kg$ $= 931.494\,32(28)\, MeV/c^2$
permittivity of free space	ϵ_0	$8.854\,187\,817 \cdots \times 10^{-12}\, F\, m^{-1}$
permeability of free space	μ_0	$4\pi \times 10^{-7}\, N\, A^{-2}$ $= 12.566\,370\,614 \cdots \times 10^{-7}\, N\, A^{-2}$
fine-structure constant	$\alpha = e^2/4\pi\epsilon_0\hbar c$	$1/137.035\,989\,5(61)$
Bohr magneton	$\mu_B = e\hbar/2m_e$	$5.788\,382\,63(52) \times 10^{-5}\, eV\, T^{-1}$
nuclear magneton	$\mu_N = e\hbar/2m_p$	$3.152\,451\,66(28) \times 10^{-8}\, eV\, T^{-1}$
Boltzmann constant	k	$1.380\,658(12) \times 10^{-23}\, J\, K^{-1}$ $= 8.617\,385(73) \times 10^{-5}\, eV\, K^{-1}$
Avogadro constant	N_A	$6.022\,136\,7(36) \times 10^{23}\, mol^{-1}$
magnetic moment of electron magnetic moment of proton magnetic moment of deuteron	$\frac{1}{2} g_S\, \mu_B$ $\frac{1}{2} g_p\, \mu_N$ $\frac{1}{2} g_d\, \mu_N$	$1.001\,159\,652\,193(10)\, \mu_B$ $2.792\,847\,39(6)\, \mu_N$ $0.857\ 438\,230(24)\, \mu_N$[59]

Table B.1: List of physical constants used in this work (taken from [60]).

Bibliography

[1] HERMES Collobration, HERMES Technical Design Report, 1993

[2] M. Düren, Habilitation Thesis, University Erlangen-Nuernberg, 1995

[3] K. Rith, Prog. Part. Nucl. Physics 49 (2002), 245-324

[4] K. Ackerstaff et al., Nucl. Instr. and Meth. A 417 (1998), 230

[5] HERMES Collobration, HERMES 97-032, 1997

[6] HERMES Collobration, HERMES 02-003, 2002

[7] A. A. Sokolov and I. M. Ternov, Sov. Phys. Doklady 8 (1964), 1203

[8] J. Buon and K. Steffen, Nucl. Instr. and Meth. A 245 (1986), 248

[9] M. Beckmann et al., Nucl. Instr. and Meth. A 479 (2002), 334

[10] look for example:
J. J. Aubert et al., Phys. Lett. B 105 (1981), 315, 322; 123 (1983), 275;
J. Ashman et al., Phys. Lett. B 206 (1988), 364; Nucl. Phys. B 328 (1989), 1

[11] F. Rathmann et al., Phys. Rev. C 58 (1998), 658;
B. v. Przewoski et al., Phys. Rev. C 58 (1998), 1897;
H. O. Meyer et al., Phys. Rev. Lett. 81 (1998), 3096

[12] D. Albers et al., Phys. Lett. 78 (1997), 1652

[13] C. Baumgarten, Ph. D Thesis, LMU München, (2000)

[14] C. Cohen-Tannoudji, B. Diu, F. Laloë, Quatum Mechanics Vol. II (1977)

[15] U. Holm and H. Ebinghaus, NIM 95 (1971), 39; Saewoong Oh, Nucl. Instr. Meth. 82 (1970), 189; W. Drewes, H. Jänsch, E. Koch and D. Fick, Phys. Rev. Lett. 50 (1983), 1759; A. D. Roberts et al., Nucl. Instr. Meth. A 322 (1992), 6

[16] R. J. Philpott, Nucl. Instr. and Meth. A 259 (1987), 317

[17] W. Gerlach and O. Stern, Z. Physik 8 (1921), 110

[18] B. Braun, Ph. D Thesis, LMU Münich, 1995

[19] K. Halbach, Nucl. Instr. Methods 169 (1980), 1

[20] Sumitomo Special Metals Company Ltd. , Enawa, Shimamotocho, Mishimagun, Osaka 618, Japan

[21] M. Sagawa et al., J. Appl. Phys. 55 (1984), 2083

[22] For a listing of materials and magnetic properties, see Table I and *Rare Earth Permanent Magnets,* VACODYM, Company Information Booklet PD-002, Vacuumschmelze GmbH, P.O.B. 2253, 63412 Hanau, Germany, p. 12

[23] L. G. Isaeva, et al., Nucl. Instr. Methods A 411 (1998), 201

[24] D. Krischel, et al., Rev. Sci. Instr. 69 (1998), 677

[25] A. Vassiliev, et al., Rev. Sci. Instr. 71 (2000), 3331

[26] ANKE Collaboration, Apparatus for Nucleon and Kaon Ejectiles, see webpage at http://ikpd15.ikp.kfa-juelich.de:8085/doc/Anke.html

[27] see for example: D. M. Nikolenko, et al., Nucl. Phys. A 684 (2001), 525

[28] D. K. Toporkov, Proc. Int. Workshop on Polarized Ion Sources and Polarized Gas Jet, February 12-17, 1990. KEK Report 90-15, p. 208; L. Dick and W. Kubischta, ibid., p.232

[29] CST GmbH, Büdinger Str. 2a, 64289 Darmstadt, Germany

[30] A. N. Dubrovin, MERMAID, User Guide

[31] H. Kolster, Ph. D Thesis, LMU München, (1998)

[32] C. Baumagarten et al., Nucl. Instr. and Methods A, 496 (2002), 263

[33] C. Baumgarten et al., Nucl. Instrum. and Meth. A, 496 (2002), 277

[34] J. C. Camparo, J. Chem. Phys. 86, Vol 3 (1987), 1533; M. Stephens, R. Rhodes and C. Wieman, J. Appl. Phys. 76, Vol 6 (1994),3479

[35] C. Baumgarten et al., Eur. Phys. J. D 18 (2002), 37

[36] A. E. Fick, Ann. Physik 94 (1855), 59

[37] The HERMES Collabiratuib, Nuclear Polarization of Molecular Hydrogen Recombined on a Non-metallic Surface, under preparation

[38] C. Baumgarten, Diploma Thesis, LMU München, (1996)

[39] A. Nass, et al., Nucl. Instr. and Methods A, 505/3 (2003), 277

[40] Zhenyu Ye, Study of Intra Beam Scattering in the stern-gerlach ABS, under preparation

[41] D. Kassen, Ph. D Thesis, University of Heidelberg, (1977)

[42] I. Simiantonakis, Diploma Thesis, University of Heidelberg, (1994)

[43] J. S. Dunham, et al., Nucl. Instr. Meth. 219 (1984), 46

[44] C. Baumgarten, et al., Nucl. Instr. Meth. A, 508(2003), 265

[45] Davide Reggiani, Private Communication

[46] A. Gade, ABS-Flow measurement with the UGFS

[47] C. Baumgarten, et al., Nucl. Instr. Meth. A 482 (2002), 606

[48] H.-G. Gaul and E. Steffens, Nucl. Instr. Meth. A 316 (1992), 297

[49] Ines Brunn, Optimization of the Magnet System of the Breit-Rabi Polarimeter and Calibration of the Target Gas Analyzer of the Hermes Experiment at Desy

[50] M. Düren, A Luminosity Monitor for the HERMES Experiment, DESY-HERMES 5/90;
T. Benisch, Diploma Thesis, University Erlangen-Nürnberg (1994);
T. Benisch, Ph. D Thesis, University Erlangen-Nürnberg (1998);
C. Weiskopf, Diploma Thesis, University Erlangen-Nürnberg (1998)

[51] S. Potashov, HERMES Internal Report 31, (1998)

[52] P. Tait, Report on the HERMES Collabration meeting at DESY, March 31st, 2003

[53] http://www3.tsl.uu.se/thep/lepto/

[54] http://www.thep.lu.se/ torbjorn/Pythia.html

[55] http://www.jlab.org/RC/

[56] Davide Reggiani, Ph. D Thesis, Universita of Ferrara (2003)

[57] Geant User's Guide,CERN

[58] Michiel Demey, Private Comunication

[59] R. B. Firestone and V. S. Shirley (Edts.), Table of Isotopes, 8th Edt., Vol. 1, Wiley Interscience, N. Y. 1996

[60] Particle Physics Booklet, July 2002

[61] Alexandre Nass, Private Comunication

List of Tables

List of Figures

Acknowledgement

It is an excitement as well as a painful thing when people enter into a new field, thus I would like to express my gratefulness to all the colleagues at HERMES, for making a friendly working atmosphere with discussions and support. Thanks to HERMES management who make this work possible.

I am particularly thankful to my supervisor, Prof. Yunxiu Ye from University of Science and Technology of China, for providing with her support throughout the past years, as well as very fruitful discussions with her advices and experience. Thanks to Associate Prof. Ji Shen from USTC, with his supervision on the design and construction of MWPC telescope for the BEPCII test beam, design and construction of the isotopic element recognizance instrument by α backscattering method. From these works, I wish that I have gained valuable experience.

This work owes a great debt to all the Hermes target group members, especially to Dr. Mark Henoch and Dr. Alexandre Nass, for their time and patience to discuss with me about my idea of Beam Loss Measurement, Dr. Paolo Lenisa, Hrachya Marukyan, Dr. Davide Reggiani, and Phil Tait for their support and help, and the former Hermes target group members for their talented work on the Hermes target.

Thanks to Haijiang Lu, Dr. Tao Chen, who made my life here enjoyable as well as their time to listen to my story about Beam Loss Measurement. Thank Elke and Haijiang for their helps on my HERMES Inclusive MC data analysis and Elke for the MC data generation. Thank Tao for his knowledge to some fields in which I have none idea and thanks for his explanations to his current work, which may help me in the future.

Thank Wolf-Dieter Nowak very much for his careful reading of this manuscript and his suggestions and comments on it.

The final thanks are to my family and my wife-to-be Wenjuan Tang for their support in my life.